

## Full-dispersion Monte Carlo simulation of phonon transport in micron-sized graphene nanoribbons

S. Mei, L. N. Maurer, Z. Aksamija, and I. Knezevic

Citation: [Journal of Applied Physics](#) **116**, 164307 (2014); doi: 10.1063/1.4899235

View online: <http://dx.doi.org/10.1063/1.4899235>

View Table of Contents: <http://scitation.aip.org/content/aip/journal/jap/116/16?ver=pdfcov>

Published by the [AIP Publishing](#)

---

### Articles you may be interested in

[Monte Carlo simulations of phonon transport in nanoporous silicon and germanium](#)

J. Appl. Phys. **115**, 024304 (2014); 10.1063/1.4861410

[Ballistic phonon thermal conductance in graphene nanoribbons](#)

J. Vac. Sci. Technol. B **31**, 04D104 (2013); 10.1116/1.4804617

[Phonon limited transport in graphene nanoribbon field effect transistors using full three dimensional quantum mechanical simulation](#)

J. Appl. Phys. **112**, 094505 (2012); 10.1063/1.4764318

[Ballistic thermoelectric properties in graphene-nanoribbon-based heterojunctions](#)

Appl. Phys. Lett. **101**, 103115 (2012); 10.1063/1.4751287

[Tunable thermal rectification in graphene nanoribbons through defect engineering: A molecular dynamics study](#)

Appl. Phys. Lett. **100**, 163101 (2012); 10.1063/1.3703756

---



**2014 Special Topics**

PEROVSKITES

2D MATERIALS

MESOPOROUS MATERIALS

BIOMATERIALS/ BIOELECTRONICS

METAL-ORGANIC FRAMEWORK MATERIALS

**AIP** | APL Materials

**Submit Today!**

# Full-dispersion Monte Carlo simulation of phonon transport in micron-sized graphene nanoribbons

S. Mei,<sup>1,a)</sup> L. N. Maurer,<sup>2</sup> Z. Aksamija,<sup>3</sup> and I. Knezevic<sup>1,b)</sup>

<sup>1</sup>Department of Electrical and Computer Engineering, University of Wisconsin-Madison, Madison, Wisconsin 53706, USA

<sup>2</sup>Department of Physics, University of Wisconsin-Madison, Madison, Wisconsin 53706, USA

<sup>3</sup>Department of Electrical and Computer Engineering, University of Massachusetts-Amherst, Amherst, Massachusetts 01003, USA

(Received 11 September 2014; accepted 12 October 2014; published online 24 October 2014)

We simulate phonon transport in suspended graphene nanoribbons (GNRs) with real-space edges and experimentally relevant widths and lengths (from submicron to hundreds of microns). The full-dispersion phonon Monte Carlo simulation technique, which we describe in detail, involves a stochastic solution to the phonon Boltzmann transport equation with the relevant scattering mechanisms (edge, three-phonon, isotope, and grain boundary scattering) while accounting for the dispersion of all three acoustic phonon branches, calculated from the fourth-nearest-neighbor dynamical matrix. We accurately reproduce the results of several experimental measurements on pure and isotopically modified samples [S. Chen *et al.*, ACS Nano **5**, 321 (2011); S. Chen *et al.*, Nature Mater. **11**, 203 (2012); X. Xu *et al.*, Nat. Commun. **5**, 3689 (2014)]. We capture the ballistic-to-diffusive crossover in wide GNRs: room-temperature thermal conductivity increases with increasing length up to roughly 100  $\mu\text{m}$ , where it saturates at a value of 5800 W/m K. This finding indicates that most experiments are carried out in the quasiballistic rather than the diffusive regime, and we calculate the diffusive upper-limit thermal conductivities up to 600 K. Furthermore, we demonstrate that calculations with isotropic dispersions overestimate the GNR thermal conductivity. Zigzag GNRs have higher thermal conductivity than same-size armchair GNRs, in agreement with atomistic calculations. © 2014 AIP Publishing LLC. [<http://dx.doi.org/10.1063/1.4899235>]

## I. INTRODUCTION

Graphene, a single layer of  $sp^2$ -bonded carbon atoms in a two-dimensional (2D) honeycomb lattice, exhibits extraordinary electrical,<sup>1,2</sup> thermal,<sup>3–5</sup> and mechanical<sup>6,7</sup> properties. Experimental measurements<sup>3,8,9</sup> of room-temperature thermal conductivity in suspended single-layer graphene (SLG) have yielded values from 2000 to 5000 W/mK. Graphene has very high thermal conductivity compared to metallic heat conductors or other carbon-based materials, such as graphite<sup>10</sup> or diamond.<sup>11</sup> The large thermal conductivity comes from the unique lattice structure and the resulting high in-plane group velocities and low lattice anharmonicity. The high thermal conductivity makes graphene a promising candidate for thermal management in nanoelectronic circuits.<sup>4,12</sup>

The graphene nanoribbon (GNR) is a form of graphene commonly envisioned in devices because it can be patterned using standard lithography.<sup>13,14</sup> GNRs can be fabricated with various widths and lengths, as well as different line-edge roughness.<sup>15–22</sup> Phonon transport in GNRs can be drastically altered by modifying the dimensions, owing to line-edge-roughness scattering and ballistic transport features.<sup>23</sup> Moreover, thermal flow in GNRs is also tunable through the choice of substrate, isotope concentration, and ribbon crystal orientation.<sup>24,25</sup> Thermal-conductivity engineering in these systems has been attracting considerable interest in recent years.<sup>12,26</sup>

Xu *et al.*<sup>27</sup> reported measurements of both temperature and length dependence of the thermal conductivity in suspended GNR samples. They reported a thermal conductivity increase with increasing length up to 9  $\mu\text{m}$  in their wide GNRs samples. Bae *et al.*<sup>28</sup> studied SiO<sub>2</sub>-supported GNR samples and found both width and length dependence of thermal conductivity. They attributed the length dependence to a ballistic-to-diffusive crossover of the heat flow. Chen *et al.*<sup>25</sup> synthesized graphene samples with modified <sup>13</sup>C composition and showed that thermal conductivity might change to half of the original value when the <sup>13</sup>C content increases to ~50%. Orientation dependence of thermal conductivity has not been observed in experiment.

Considerable theoretical work has been done on thermal transport in GNRs. Aksamija and Knezevic studied the width and orientation dependence of thermal conductivity for both suspended<sup>29</sup> and supported<sup>30</sup> GNRs by solving the phonon Boltzmann transport equation (PBTE) under the relaxation time approximation (RTA), with a specular parameter to account for boundary roughness. Earlier, Nika *et al.*<sup>31</sup> also found a strong width dependence stemming from edge roughness by solving the PBTE under the RTA. The nonequilibrium Green's function (NEGF) technique<sup>32,33</sup> has also been employed to study thermal transport in GNRs.<sup>34–43</sup> However, these studies do not account for phonon-phonon scattering, which is very important in suspended graphene. Recent work by Luisier<sup>44</sup> is a promising advance towards solving the problem of phonon-phonon interactions at the level of NEGF. Molecular

<sup>a)</sup>Electronic mail: smeid4@wisc.edu

<sup>b)</sup>Electronic mail: knezevic@enr.wisc.edu

dynamics (MD) simulations can account for edge roughness, isotope composition, and size dependence. The effects of length,<sup>45–48</sup> width,<sup>45,46,49,50</sup> isotope concentration,<sup>51,52</sup> edge roughness,<sup>49,53</sup> and chirality<sup>45,50,54</sup> on thermal transport in GNRs have been extensively studied using MD. However, a major drawback is that the computational burden limits the sample dimensions to a few nanometers. Therefore, these calculations do not correspond very well with experimental conditions, where long and wide samples are employed.

In this paper, we analyze phonon transport in GNRs with real-space edges and micron-sized, experimentally relevant widths and lengths ( $\sim 100\text{ nm}–100\text{ }\mu\text{m}$ ) at temperatures up to 600 K. To that end, we developed a full-dispersion ensemble Monte Carlo simulation of phonon transport. As there are unique challenges associated with a full-dispersion phonon Monte Carlo (PMC) algorithm for a non-cubic system with real-space edges, we present the technique in detail. Scattering from the edges, phonon-phonon, isotope, and grain boundary scattering (for polycrystalline samples) are included in the simulation. We accurately reproduce a number of experimental measurements on pristine and isotopically modified graphene by Chen *et al.*<sup>9,25</sup> and Xu *et al.*<sup>27</sup> We capture the ballistic-to-diffusive crossover at room temperature, and show that GNRs are in the quasiballistic transport regime up to lengths in excess of  $100\text{ }\mu\text{m}$ , which is considerably longer than most experimental samples. Consequently, the true upper limit to thermal conductivity is higher than previously reported.<sup>55</sup> In agreement with atomistic calculations, we also show that the thermal conductivity of zigzag GNRs (ZGNRs) is higher than that of armchair GNRs (AGNRs), when both are calculated with full phonon dispersions. We also show that the isotropic-dispersion simulation overestimates thermal conductivity in GNRs, and the discrepancy is large in narrow GNRs and at low temperatures.

The paper is organized as follows. In Sec. II, we present the algorithm for 2D PMC in GNRs with full phonon dispersions in the presence of edge roughness and other relevant scattering mechanisms. In Sec. III, we compare the simulation data with experiment for wide GNRs (Sec. III B), demonstrate the ballistic-to-diffusive crossover in the length dependence of thermal conductivity (Sec. III C), investigate the role of isotope abundance on thermal transport (Sec. III D), analyze the width-dependence of the thermal conductivity in GNRs with edges (Sec. III E), and finally demonstrate the importance of accounting for the full phonon dispersion as opposed to isotropic relationships when working on thermal transport (Sec. III F). We conclude with Sec. IV.

## II. PHONON MONTE CARLO METHOD WITH FULL DISPERSIONS

Phonons are the main carriers of heat in graphene.<sup>23,56</sup> In a system where the characteristic length of the domain of interest is much larger than the phonon coherence length and the time scale is much longer than the phonon relaxation time, we can treat phonons as semiclassical particles.<sup>57,58</sup> Under these conditions, the phonon transport behavior is governed by the phonon Boltzmann transport equation. The PBTE describes how the phonon distribution function  $n_b(\mathbf{r}, \mathbf{q}, t)$  for a given

phonon branch  $b$  depends on time  $t$ , location  $\mathbf{r}$ , and phonon wave vector  $\mathbf{q}$ . The PBTE has the ability to capture both equilibrium and non-equilibrium phenomena and is given by

$$\frac{\partial n_b(\mathbf{r}, \mathbf{q}, t)}{\partial t} + \mathbf{v}_{b,\mathbf{q}} \cdot \nabla_{\mathbf{r}} n_b(\mathbf{r}, \mathbf{q}, t) = \left. \frac{\partial n_b(\mathbf{r}, \mathbf{q}, t)}{\partial t} \right|_{\text{scat}}. \quad (1)$$

Here,  $\mathbf{v}_{b,\mathbf{q}} = \nabla_{\mathbf{q}} \omega_{b,\mathbf{q}}$  is the phonon group velocity ( $\omega_{b,\mathbf{q}}$  is the phonon angular frequency in branch  $b$  at wave vector  $\mathbf{q}$ ). The PBTE can be solved using deterministic techniques,<sup>29,30,59–70</sup> with the collision operator usually treated in the RTA<sup>29,30,59–65</sup> or evaluated iteratively.<sup>67–70</sup> Alternatively, the PBTE can be solved using a stochastic phonon Monte Carlo method, where a large ensemble of phonons is tracked in real space as they undergo periods of free flight interrupted by scattering events. The PMC method has been successfully applied to study thermal transport in various nanostructures such as membranes<sup>71–76</sup> and nanowires,<sup>72,77–80</sup> in Si<sup>71–79,81</sup> and a number of other materials.<sup>78,80,82–86</sup> PMC has proven to be an effective tool to study nanoscale thermal transport in systems near equilibrium.<sup>74,86–89</sup> It is also straightforward to include nontrivial geometries, such as rough boundaries or edges, in PMC.<sup>43,80,90</sup>

The starting point of PMC is equilibrium. In equilibrium, the phonon distribution function reduces to the Bose-Einstein (BE) distribution,  $\langle n_{BE} \rangle$ , describing the average occupation of a phonon state

$$\langle n_{BE}(\omega, T) \rangle = \frac{1}{e^{\frac{\hbar\omega}{k_B T}} - 1}. \quad (2)$$

In the expression,  $k_B$  is the Boltzmann constant,  $\hbar\omega$  is the energy level associated with the phonon state, and  $T$  is the absolute temperature. Out of equilibrium, the concept of a local and instantaneous temperature  $T(\mathbf{r}, t)$  and the phonon dispersion relation  $\omega_{b,\mathbf{q}}$  will be used to connect the phonon distribution  $n_b(\mathbf{r}, \mathbf{q}, t)$  to Eq. (2).

Figure 1 shows a flowchart of the PMC simulation. We first specify the simulation domain, according to the desired

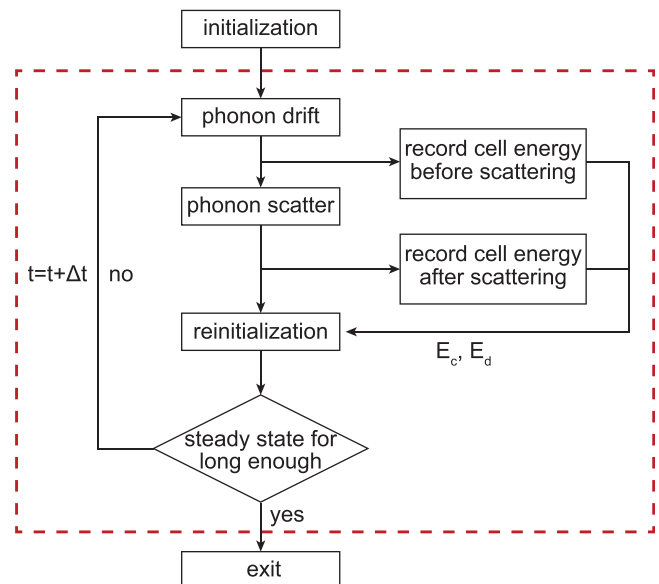


FIG. 1. Flowchart of the PMC simulation. Transport kernel is inside the dashed box.

simulation parameters, such as the ribbon size and temperature boundary conditions. The domain is divided into cells, whose size is chosen according to the criteria we discuss in Sec. II B. Initialization of the phonon ensemble, described in Sec. II C, requires information on the phonon dispersion and the phonon density of states (PDOS), which are pre-calculated using the method described in Sec. II A. After initialization, we enter the transport kernel (enclosed in a dashed box in Fig. 1) where time is discretized with a small step  $\Delta t$ . In PMC simulations, the timestep  $\Delta t$  is small enough that a phonon is unlikely to scatter more than once within it, so drift (free flight) of phonons and scattering are separated:<sup>71,77–80,87,90</sup> phonons first drift and potentially scatter from real-space edges during time  $\Delta t$ , and then we treat all the scattering events cumulatively, for the entire ensemble, at the end of the step. Energy of all phonons in a cell is recorded before and after the scattering process routine, as the inelastic processes do not conserve the energy of individual phonons; a mismatch in energy is addressed by creating/deleting additional phonons, as described in Sec. II F. In Secs. II A–II G, we describe the components of the full-dispersion PMC in detail.

### A. Phonon dispersion and density of states

The phonon dispersion relation for a given branch  $b$  describes the relationship between the angular frequency  $\omega$  and the wave vector  $\mathbf{q}$  in the first Brillouin Zone (1BZ).<sup>91</sup> It reflects the symmetry of the underlying lattice. From dispersion, we calculate properties such as the PDOS and group velocity. In previous PMC work,<sup>71–74,77–84,86,87,90</sup> isotropic relationships were often used to approximate the dispersion. However, the phonon dispersion relations of graphene are quite anisotropic.<sup>29,70,92–94</sup> Furthermore, each GNR has a specific orientation, and keeping the anisotropy in dispersion is essential for describing transport in differently oriented ribbons. As a result, we include full phonon dispersions in this work.

The phonon dispersion relations are calculated with the empirical dynamical matrix method including fourth-nearest-neighbors (4NN) proposed by Saito *et al.*<sup>95</sup> We first write the general equation of motion for the displacement of the  $i$ th atom as

$$M_i \ddot{\mathbf{u}}_i = \sum_j K^{ij} (\mathbf{u}_j - \mathbf{u}_i) \quad (i = 1, \dots, N), \quad (3)$$

where  $M_i$  is the mass of the  $i$ th atom and  $K^{ij}$  is the interaction force tensor between the  $i$ th and the  $j$ th atom. Then, with the Bloch theorem<sup>96</sup> we can change the variable to the normal mode displacements  $\mathbf{u}_q^i$  because  $\mathbf{u}_i = \frac{1}{\sqrt{N_\Omega}} \sum_{\mathbf{q}'} \mathbf{u}_{\mathbf{q}'}^i \exp[-i(\mathbf{q}' \cdot \mathbf{R}_i - \omega t)]$ . Here,  $N_\Omega$  is the number of wave vectors  $\mathbf{q}'$  in the 1BZ and  $\mathbf{R}_i$  denotes the original position of the  $i$ th atom. After further simplification and combination of terms, we obtain an eigenvalue problem

$$\mathcal{D}(\mathbf{q}) \mathbf{u}_q = 0, \quad (4)$$

where  $\mathcal{D}(\mathbf{q})$  is the dynamical matrix and the associated eigenvalues are  $\omega^2(\mathbf{q})$ .

In graphene, there are two atoms, A and B, in a unit cell and the atoms can move in three dimensions,<sup>97</sup> thus we get a  $6 \times 6$  dynamical matrix. After solving its eigenvalue problem for each  $\mathbf{q}$ , we get six phonon branches: transverse acoustic (TA), longitudinal acoustic (LA), flexural acoustic (ZA), transverse optical (TO), longitudinal optical (LO), and flexural optical (ZO). The force constants we used are parametrized to fit both experimental findings<sup>98</sup> and first-principles calculations.<sup>92</sup> The force constant for the radial, transverse in-plane, and transverse out-of-plane directions for the  $n$ th ( $n = 1, 2, 3, 4$ ) nearest neighbors ( $\phi_r^{(n)}$ ,  $\phi_{ii}^{(n)}$ , and  $\phi_{to}^{(n)}$ , respectively) are shown in Table I.

The obtained dispersion relations are shown in Fig. 2. Optical branches have relatively flat dispersions, thus phonons in these branches have very small group velocities. Further, the energies associated with optical phonons are relatively large, so, based on Eq. (2), the occupation of those phonon states is low at temperatures of interest here (up to 600 K). Owing to these reasons combined, optical phonons make a negligible contribution to the thermal conductivity of graphene.<sup>29</sup> TA and LA phonons have almost linear dispersions and large group velocities near the  $\Gamma$  point, thus they were long believed to be the main carriers of heat.<sup>10,99</sup> ZA phonons have a quadratic dispersion and therefore nearly zero group velocity near the  $\Gamma$  point. However, they are numerous, and recent studies have shown that they make a large contribution to the lattice thermal conductivity of suspended graphene.<sup>68–70,100</sup> Therefore, we include all three acoustic branches in this work.

PDOS in graphene describes the number of states per unit angular frequency and area that are supported by the material. PDOS is essential in generating phonons in the simulation and also enters some of the scattering rate expressions. The general expression for PDOS of branch  $b$  in a 2D system is<sup>101</sup>

$$D_b(\omega) d\omega = \frac{1}{(2\pi)^2} \int_{\omega_{b,q} \in [\omega, \omega + d\omega]} d^2q. \quad (5a)$$

Let  $L_{b,\omega}$  denote the length of the isoenergy curve for branch  $b$  and angular frequency  $\omega$ ; then, the PDOS for branch  $b$  can be expressed by

$$D_b(\omega) = \frac{1}{(2\pi)^2} \int \frac{dL_{b,\omega}}{v_{b,\omega}}. \quad (5b)$$

Here,  $v_{b,\omega}$  is the group velocity magnitude,  $v_{b,q}$ , evaluated at the  $\mathbf{q}$  that satisfies  $\omega = \omega_{b,q}$ . We evaluate Eq. (5b) with a numerical method proposed by Gilat and Raubenheimer,<sup>102</sup>

TABLE I. Force constants for 2D graphene in units of 10N/m. The subscripts  $r$ ,  $ii$ , and  $to$  refer to the radial, transverse in-plane, and transverse out-of-plane directions, respectively.

Radial	In-plane	Out-of-plane
$\phi_r^{(1)} = 41.800$	$\phi_{ii}^{(1)} = 15.200$	$\phi_{to}^{(1)} = 10.200$
$\phi_r^{(2)} = 7.600$	$\phi_{ii}^{(2)} = -4.350$	$\phi_{to}^{(2)} = -1.080$
$\phi_r^{(3)} = -0.150$	$\phi_{ii}^{(3)} = 3.390$	$\phi_{to}^{(3)} = 0.995$
$\phi_r^{(4)} = 0.690$	$\phi_{ii}^{(4)} = -0.190$	$\phi_{to}^{(4)} = -0.550$

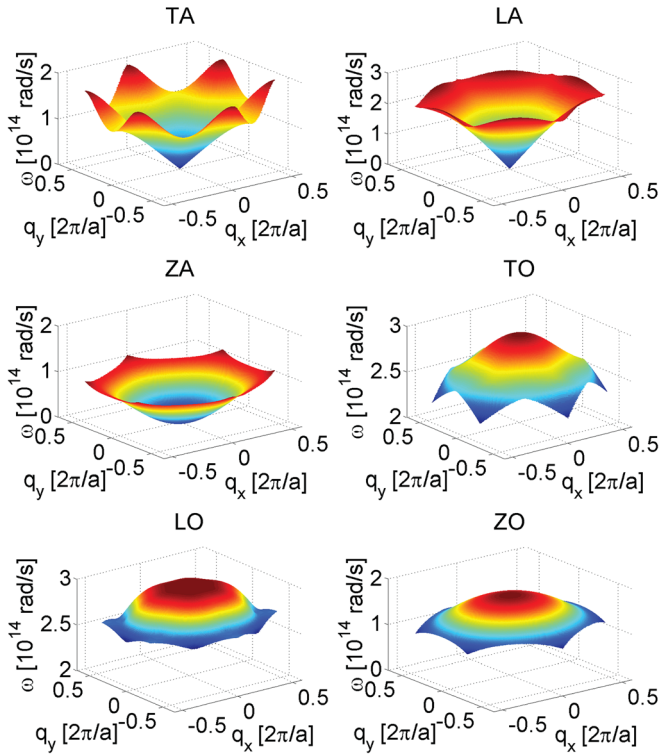


FIG. 2. Dispersion curves for the TA, LA, ZA, TO, LO, and ZO phonon branches in single-layer graphene, calculated from the empirical dynamical matrix method including 4th nearest neighbors.

modified for 2D. The idea is that we can approximate the dispersion curve with piecewise linear segments, and the error would become arbitrarily small as we increase the number of segments. We partition the first Brillouin zone (1BZ) into  $2000 \times 4000$  grid cells. Within each grid cell, this small ( $dq < 6 \times 10^{-4} \text{ m}^{-1}$ ), the isoenergy curve segment is a line whose length we can readily calculate; we also assume that  $v$  is constant everywhere along the segment and calculate it numerically from finite differences. We can accurately evaluate the integral in Eq. (5b) by summing up all contributions from different linear segments.

The method described above would allow us to calculate the PDOS at one  $\omega$  value. To obtain the full spectrum, we calculate PDOS at a discrete set of points and interpolate between them. The interpolation error can always be reduced by increasing the number of points. Let  $\omega_{\max}$  represent the maximal frequency in the acoustic branches according to the dispersion relations. We divide the frequency interval between 0 and  $\omega_{\max}$  into equal parts with  $\Delta\omega = \text{ceiling}(\frac{\omega_{\max}}{N_{\text{int}}})$ . Here,  $N_{\text{int}}$  is the number of intervals. We choose the central frequency of each interval ( $\omega_{c,i} = \frac{2i-1}{2} \Delta\omega$ ) to evaluate the PDOS. This discretization is also used in phonon generation, as we will discuss later.  $\Delta\omega = 10^{11} \text{ rad/s}$  and  $N_{\text{int}} = 2500$  have been shown to provide good accuracy without being too computationally expensive. Figure 3 shows the calculated PDOS for the three acoustic branches. As we see from the figure, the ZA branch has a non-zero PDOS at  $\omega = 0$  because of its quadratic dispersion near the  $\Gamma$  point. We are interested in the temperature range up to 600 K, therefore, from Eq. (2), the relevant frequency range is  $\omega \in [0, 5 \times 10^{13}] \text{ rad/s}$ . Note that

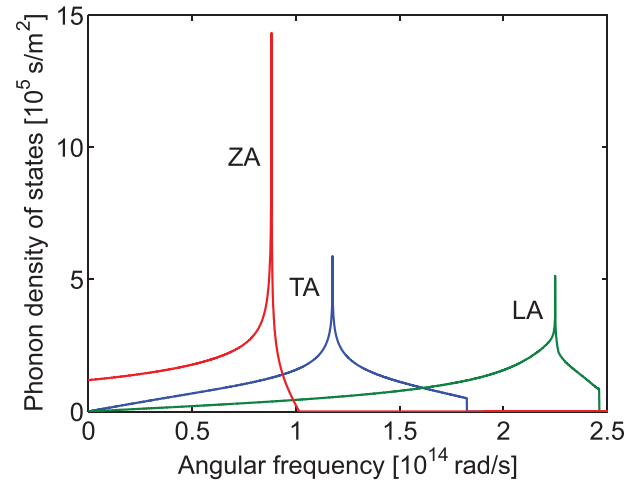


FIG. 3. Phonon density of states (PDOS) for TA, LA, and ZA branches in graphene, calculated following the Gilat-Raubenheimer method.<sup>102</sup>

the ZA PDOS is overwhelmingly larger than that of TA and LA branches in this range, making the ZA phonons the most numerous.

## B. Simulation domain

The simulation domain is a ribbon of width  $W$  and length  $L$  in 2D, as shown in Fig. 4; the ribbon generally has edges, so the domain is not strictly rectangular. Phonons are only allowed to transport in-plane. We follow previous work<sup>71,72,74,77-80</sup> and divide the length ( $x$  direction) into several cells. Two ends of the ribbon are connected to thermal reservoirs with constant temperatures  $T_h$  and  $T_c$  (hot and cold, respectively). In the steady state and diffusive regime, a linear temperature profile should develop inside the ribbon. If we choose a temperature difference  $\Delta T = T_h - T_c$  and a number of cells  $N_c$  such that the temperature variation across a cell is small, we can employ the approximation of local

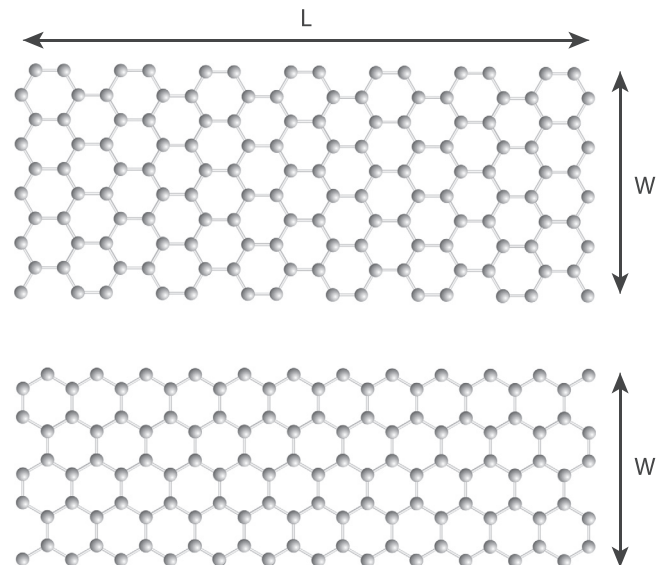


FIG. 4. Schematic of the simulation domain of width  $W$  and length  $L$ . (Top) Armchair GNR. (Bottom) Zigzag GNR.

equilibrium, with a cell-specific temperature  $T_i$ ,  $i$  being the cell index. We assume the phonons inside a cell to be uniformly spatially distributed and follow the equilibrium BE distribution over energy according to  $T_i$ . In a typical simulation,  $\Delta T$  is 20–40 K and  $N_c$  varies from 50 to 100, depending on the ribbon length. We make sure that the temperature drop in each cell is small ( $\frac{\Delta T}{N_c} < 0.5$  K), to make sure the local equilibrium approximation is valid.

## C. Initialization

### 1. Initial temperature profile

To achieve a steady state faster, we initialize the phonons in each cell according to the expected linear temperature profile. The initial temperature in the  $i$ th cell is  $T_i = T_l - \frac{i-1}{N_c-1}(T_r - T_l)$ , where  $N_c$  is the total number of cells in the ribbon, as before.  $T_l$  and  $T_r$  are the temperatures at the left and right ends of the ribbon; their values are fixed at the temperatures of the reservoirs ( $T_h$  or  $T_c$ ). The total energy associated with the  $i$ th cell is then

$$\mathcal{E}_i = A_i \sum_b \int D_b(\omega) \langle n_{\text{BE}}(\omega, T_i) \rangle \hbar \omega d\omega, \quad (6)$$

where  $A_i$  is the area of the  $i$ th cell in real space and the sum is over all three phonon branches. We can calculate the expected number of phonons in the cell as

$$\mathcal{N}_{i, \text{exp}} = A_i \sum_b \int D_b(\omega) \langle n_{\text{BE}}(\omega, T_i) \rangle d\omega. \quad (7)$$

In simulations where the sample size is large (on the order of microns) or the temperature is not very low (a few hundred Kelvin), the expected number of phonons  $\mathcal{N}_{i, \text{exp}}$  can be very large ( $10^7$ – $10^9$ ) and is computationally expensive to keep track of. A weighting factor  $W$  is often introduced<sup>71,78</sup> to reduce the number of simulation particles to a tolerable range (typically  $10^5$ – $10^6$ ). As we have mentioned, in 2D materials like graphene, the number of ZA phonons is overwhelmingly larger than that of TA and LA phonons (see Fig. 3). As a result, if we use a uniform weighting factor  $W$ , the number of TA and LA phonons would be too small to be statistically significant and their contribution would be undersampled. Therefore, in order to better address the contributions from the in-plane modes, we use a different weighting factor  $W_b$  for each phonon branch  $b$ . In a typical simulation,  $W_{\text{ZA}}$  is often one order of magnitude larger than  $W_{\text{TA}}$  and  $W_{\text{LA}}$ . With the weighting factor, we control the number of phonons in each cell to be around  $10^4$ – $10^5$ . Considering the weighting factor, the total energy of the ensemble of particles used in the simulation becomes

$$E_i = A_i \sum_b \int D_b(\omega) \frac{\langle n_{\text{BE}}(\omega, T_i) \rangle}{W_b} \hbar \omega d\omega. \quad (8a)$$

Since there is no analytical expression for the PDOS, we evaluate Eq. (8a) numerically using the same  $\omega$  discretization as mentioned in Sec. II A,

$$E_i = A_i \sum_b \sum_{j=1}^{N_{\text{int}}} D_b(\omega_{c,j}) \frac{\langle n_{\text{BE}}(\omega_{c,j}, T_i) \rangle}{W_b} \hbar \omega_{c,j} \Delta\omega. \quad (8b)$$

Here,  $\omega_{c,j}$  represents the central frequency in the  $j$ th frequency interval. Note that  $\frac{\langle n_{\text{BE}}(\omega_{c,j}, T_i) \rangle}{W_b}$  plays the role of the expectation number of simulated phonons in branch  $b$  and with angular frequency  $\omega_{c,j}$  in a cell with temperature  $T_i$ .

We initialize each cell by generating phonons, one by one, following the desired distribution according to the temperature of the cell and adding them to the cell. Since we have assumed local equilibrium inside a cell, we can put each generated phonon in a random position inside the cell. We keep generating phonons in the cell until the ensemble in the cell has the effective total energy  $E_i$ , Eq. (8b). However, since our process of generating phonons is independent of how much energy is already in the cell, we cannot enforce the exact  $E_i$  and respect the phonon distribution simultaneously. Compared with a small offset in energy, violating the distribution is much worse. As a result, we do not enforce energy in the cell exactly and we stop generating phonons once the energy in the cell  $E_{i, \text{actual}}$  falls within  $(E_i - \frac{\hbar\omega_{\text{max}}}{2}, E_i + \frac{\hbar\omega_{\text{max}}}{2})$ . As the accumulation of the offset energy over the course of the simulation may lead to big problems, we record the offset  $E_{i, \text{offset}} = E_i - E_{i, \text{actual}}$  and add it to the desired cell energy the next time we initialize the cell (see more detail in Sec. II F).

### 2. Single phonon generation

To generate a phonon ensemble with a proper distribution over angular frequency, we should make sure that: (1) the frequency distribution follows the BE distribution at the local temperature, (2) for a phonon with certain angular frequency, the wave vector is chosen so that  $\omega_{b,q}$  falls on the desired branch of the dispersion curve. A schematic of the phonon generation process is shown in Fig. 5.

Before phonon generation, we first need to specify the local temperature of the cell this phonon is in. Sometimes the temperature is assigned (see Sec. II C 1); other times, we need to find the temperature numerically. The relationship between the total energy  $\mathcal{E}$  and temperature  $T$  of a cell of area  $A$  is given by [same as in Eq. (6)]

$$\mathcal{E} = A \sum_b \int D_b(\omega) \langle n_{\text{BE}}(\omega, T) \rangle \hbar \omega d\omega. \quad (9)$$

We compute the total energy of the cell by summing up all the phonon energies, making sure each numerical phonon's energy is multiplied by the branch-appropriate weight, then use Newton's iterative method to get the local temperature based on Eq. (9).

Once the temperature is known, we can calculate the frequency cumulative distribution function (CDF) according to  $T$ . Here, we use the same frequency discretization as in Sec. II A. The  $i$ th number  $F_i$  in the normalized CDF table represents the probability of finding a phonon with  $\omega < \omega_{i, \text{max}}$ , where  $\omega_{i, \text{max}}$  stands for the maximal frequency in the  $i$ th frequency interval.

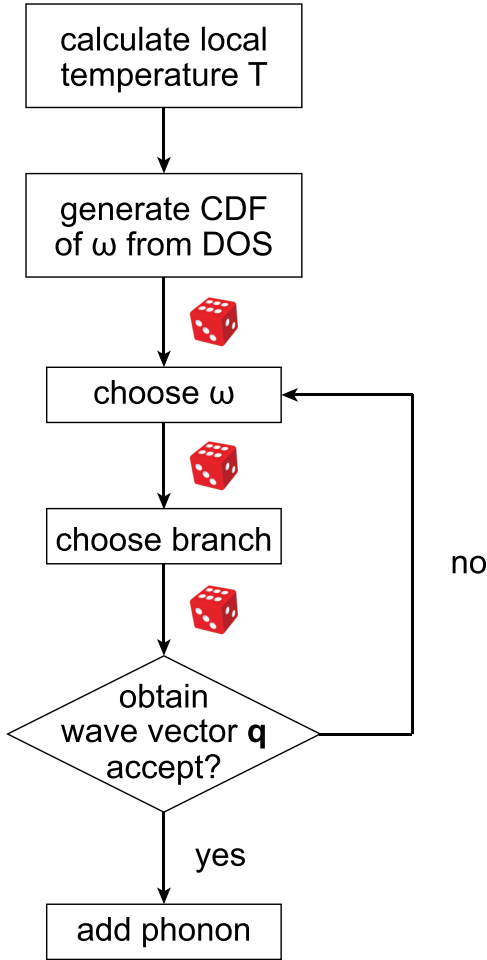


FIG. 5. Flowchart showing the steps for generating a single phonon in the numerical ensemble of a cell at a given temperature. Dice indicate the use of random numbers.

$$F_i(T) = \frac{\sum_b \sum_{j=1}^i \langle n_{\text{BE}}(\omega_{c,j}, T) \rangle D_b(\omega_{c,j}) / W_b}{\sum_b \sum_{j=1}^{N_{\text{int}}} \langle n_{\text{BE}}(\omega_{c,j}, T) \rangle D_b(\omega_{c,j}) / W_b}. \quad (10)$$

The sum goes from interval 1 to interval  $i$  in the numerator, and from 1 to  $N_{\text{int}}$  in the denominator. The table is automatically normalized as  $F_{N_{\text{int}}}(T) = 1$ . PDOS in the expression is calculated from the full dispersion as described in Sec. II A. To complete the table, we manually set  $F_0(T) = 0$ , meaning that all phonons have positive energy. The CDF for phonons at 300 K is shown in Fig. 6.

With the table formed, we draw a random number  $R_1$  and look for the interval  $i$  satisfying  $F_{i-1} < R_1 < F_i$  with the bisection algorithm. We decide the frequency of this phonon falls in the  $i$ th interval and the actual frequency is determined with another random number  $R_2$ ,  $\omega = \omega_{c,i} + (2R_2 - 1) \frac{\Delta\omega}{2}$ .

After an  $\omega$  is chosen, we draw a third random number  $R_3$  to choose the phonon branch  $b$ . The probability of a phonon with  $\omega$  being in branch  $b$  is proportional to  $D_b(\omega)$ , therefore, we have

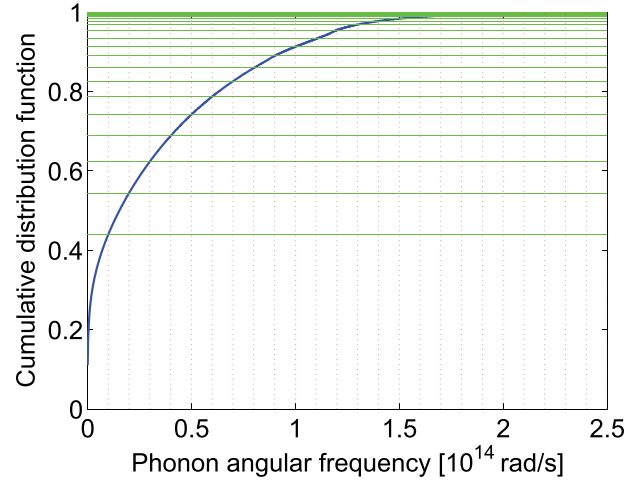


FIG. 6. Cumulative distribution function of phonon frequency at 300 K. The frequency range  $\omega \in [0, 2.5 \times 10^{14}]$  rad/s was divided into  $N_{\text{int}} = 2500$  equal intervals in the numerical calculation.

$$b = \begin{cases} \text{TA}, & R_3 < f_{\text{TA}}(\omega) \\ \text{LA}, & f_{\text{TA}}(\omega) < R_3 < f_{\text{TA}}(\omega) + f_{\text{LA}}(\omega), \\ \text{ZA}, & \text{otherwise.} \end{cases} \quad (11)$$

where  $f_b(\omega) = \frac{D_b(\omega)}{W_b} / \sum_{b'} \frac{D_{b'}(\omega)}{W_{b'}}$  is the normalized probability of being in branch  $b$  for the chosen frequency  $\omega$  with the weighting taken into consideration.

The next step is generating the phonon wave vector,  $\mathbf{q}$ , for the  $\omega$  and  $b$  we already found, which we do by using a rejection technique. The procedure is technically complex, so the details have been relegated to Appendix A.

#### D. Phonon drift and edge scattering

After initialization, we enter the transport kernel. As mentioned at the beginning of Sec. II, we treat phonon drift and scattering independently. At each step, we first let the phonons drift inside the ribbon with their specified group velocities. The time step  $\Delta t$  is chosen according to the criteria explained later, in Sec. II E. At the end of each step, the phonon position is updated as  $\mathbf{r}_{\text{end}} = \mathbf{r}_{\text{start}} + \mathbf{v}_g \Delta t$  unless it hits a boundary in the meantime.

In this work, we simulate GNRs with real-space edges, as shown in Fig. 4. Two different rough edges are considered: the perfect armchair edge and the zigzag edge. Although the structure is perfectly periodic, the edges effectively introduce back-scattering of phonons and reduce the thermal conductivity, similar to rough edges. Phonons reflect specularly once they hit the edge, and multiple reflection might happen within a time step. Since boundary scattering is elastic, it is essential that, after reflection, the new wave vector and the old wave vector end up on the same isoenergy curve, i.e.,  $\omega_{b,q_{\text{new}}} = \omega_{b,q_{\text{old}}}$ . Both edges we used share the same symmetry as the phonon dispersion; therefore, this requirement is automatically met with specular reflection.

It has been shown that, when the width of GNRs is large, thermal conductivity is very weakly dependent on the width

and gradually saturates at the value where there is no edge roughness.<sup>27,28</sup> We use flat-edge GNRs (rectangularly shaped) with specular reflection to recover the bulk properties in our simulation, as specular reflection from flat edges does not alter the phonon velocity component along the GNR and thus introduces no resistance. As there is no width dependence in the calculated thermal conductivity of the GNRs with flat edges, the width can be really small to save simulation time.

## E. Phonon scattering

We include multiple scattering mechanisms in the phonon Monte Carlo simulation of suspended graphene: three-phonon (umklapp and normal), isotope, and grain boundary scattering. The total scattering rate for a given  $\omega$  and  $b$  is as follows:

$$\tau_b^{-1}(\omega) = \sum_i \tau_{b,i}^{-1}(\omega), \quad (12)$$

where  $\tau_b^{-1}$  is the total scattering rate and  $\tau_{i,b}^{-1}$  is the contribution from the  $i$ th mechanism. A description of different scattering mechanisms and their rates is given in detail in Appendix B. Edge roughness scattering is explicitly taken care of during the drift process (see Sec. II D), thus not discussed here. In order to treat the drift and scattering processes separately and scatter all phonons cumulatively at the end of the time step, the time step has to be short enough that multiple non-edge scattering events are unlikely. For a phonon with angular frequency  $\omega$  in branch  $b$ , whose scattering rate is  $\tau_b^{-1}(\omega)$ , the probability of scattering after time  $\Delta t$  is<sup>96</sup>

$$p_{b,\text{scat}}(\omega) = 1 - \exp[-\Delta t \cdot \tau_b^{-1}(\omega)]. \quad (13)$$

Thus, our criterion of a small enough step is that the average probability of scattering for all phonons,  $\overline{p_{\text{scat}}}$ , be small enough. In practice, we found that  $\overline{p_{\text{scat}}} < 1\%$  is a good criterion for choosing the time step  $\Delta t$ . As a result, the time step would vary for simulations at different temperatures, as the rates are temperature dependent. For suspended graphene at 300 K, we use  $\Delta t = 0.1$  ps.

After each time step (upon completion of the drift routine), for each phonon we calculate the probability of having been scattered during the previous step from Eq. (13). Note that scattering rates are temperature-dependent, so we should update the temperature in each cell after the drift before calculating the probabilities. We then use a random number  $r_1$  to decide whether the phonon would actually scatter. If  $r_1 > p_{b,\text{scat}}$ , nothing happened and we move on to the next phonon. If  $r_1 \leq p_{b,\text{scat}}$ , the phonon scattered. As  $\Delta t$  is short enough so that we do not expect multiple scattering events during one step, the probability of encountering the  $i$ th scattering mechanism is approximately proportional to its rate,

$$p_{b,\text{scat},i}(\omega) = 1 - \exp[-\Delta t \cdot \tau_{b,i}^{-1}(\omega)] \approx \Delta t \cdot \tau_{b,i}^{-1}(\omega). \quad (14)$$

We use another random number  $r_2$  to choose the mechanism in a similar way to choosing the phonon branch in Sec. II C

2. Once the mechanism is chosen, we scatter the phonon accordingly. We treat the scattering events differently according to whether they are inelastic (phonon-phonon scattering) or elastic (all other mechanisms).

For elastic scattering, we keep the phonon branch and energy, but randomly find a new wave vector and group velocity according to the dispersion relation. The algorithm is described in Appendix A.

For inelastic (phonon-phonon) scattering, we treat the collision effectively by replacing the phonon with a random new phonon from the phonon pool. The energy is not enforced for a single phonon in the process, but collectively for the whole cell at the end of the step. We need to make sure that the phonons generated after inelastic scattering follow the same distribution as the phonons being replaced, which is different from the equilibrium BE distribution we used in generating phonons in the initialization process, because the scattering rate is energy-dependent. As a result, we need a modified CDF to generate phonons after the phonon-phonon interaction

$$F_{\text{mod},i}(T) = \frac{\sum_b \sum_{j=1}^i N_j(T) \cdot p_{b,U}(\omega_{c,j})}{\sum_b \sum_{j=1}^{N_{\text{int}}} N_j(T) \cdot p_{b,U}(\omega_{c,j})}, \quad (15)$$

where  $N_j(T) = \langle n_{\text{BE}}(\omega_{c,j}, T) \rangle D_b(\omega_{c,j}) / W_b$  is the average number of simulation particles (“numerical phonons”) in the  $j$ th energy interval and  $p_{b,U}(\omega_{c,j})$  is the probability of a phonon in branch  $b$  suffering from umklapp scattering during the step. A typical modified CDF is shown in Fig. 7 for 300 K and a timestep of 0.1 ps. We can see that, in the modified CDF, the percentage of phonons with very small energy is reduced because these phonons do not undergo scattering events frequently and thus have a small probability of being replaced (or being generated after scattering). Other than the different CDF function, the phonon generation process is the same as described in Sec. II C 2. With the modified distribution, we conserve the energy in an average sense. However, sometimes the number of phonons in a cell is not large

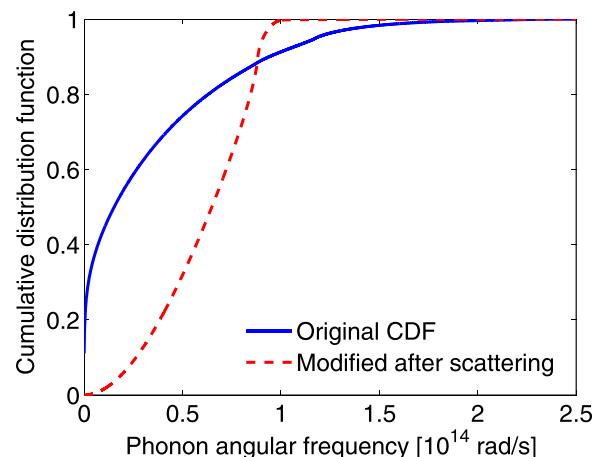


FIG. 7. A typical modified (post-scattering) CDF, Eq. (15), and the original CDF, Eq. (10), at 300 K.

enough to provide adequate statistics; therefore, to conserve the energy explicitly, we add a reinitialization process after the scattering routine, as described in Sec. II F below.

### F. Reinitialization

As mentioned in Sec. II E, our treatment of inelastic scattering does not conserve energy precisely in a cell. We enforce the conservation more exactly through ensemble reinitialization.

During drift, phonons might cross cell boundaries, and therefore change the total energy in each cell; the energy of phonons that drifted in/out has to be added/subtracted before entering the scattering routine. We record the cell energy just after the phonons finish drift in an array  $E_{i,\text{prescat}}$ . As we mentioned in Sec. II C, we have another array  $E_{i,\text{offset}}$  recording the offset energy from our last attempt at enforcing energy conservation. So now the desired energy after scattering is  $E_{i,d} = E_{i,\text{prescat}} + E_{i,\text{offset}}$ . Then, we can scatter the phonons as described in Sec. II E and calculate and record the actual cell energy  $E_{i,\text{afterscat}}$ .

As explained in Sec. II C, to respect the phonon distribution, we do not insist on getting the exact desired energy  $E_{i,d}$  after reinitialization. We would only enforce that the cell energy  $E_i$  get into the range  $[E_{i,d} - \frac{\hbar\omega_{\text{max}}}{2}, E_{i,d} + \frac{\hbar\omega_{\text{max}}}{2}]$ . The initial cell energy in the reinitialization process is  $E_i = E_{i,\text{afterscat}}$ . For each cell  $i$ , we compare  $E_i$  and  $E_{i,d}$ . If  $E_i \in [E_{i,d} - \frac{\hbar\omega_{\text{max}}}{2}, E_{i,d} + \frac{\hbar\omega_{\text{max}}}{2}]$ , we consider this cell good and move on to the next one. If  $E_i > E_{i,d} + \frac{\hbar\omega_{\text{max}}}{2}$ , we would randomly choose one phonon in the cell and delete it. After the deletion, the new energy in the cell is  $E_i^{\text{new}} = E_i^{\text{old}} - \hbar\omega_0$ , where  $\hbar\omega_0$  is the energy carried by the deleted phonon. Then, we compare  $E_i^{\text{new}}$  and  $E_{i,d}$  again and keep this random deletion until  $E_i^{\text{new}}$  falls in the desired range. If  $E_i < E_{i,d} - \frac{\hbar\omega_{\text{max}}}{2}$ , we generate a phonon from the equilibrium distribution and add it to a random place in the cell (note that here the CDF is the original CDF as described in Sec. II C). The new cell energy after addition is  $E_i^{\text{new}} = E_i^{\text{old}} + \hbar\omega_0$ , where  $\hbar\omega_0$  is the energy carried by the added phonon. Similarly, we keep adding phonons until the final  $E_i$  falls in the appropriate range. After all cells have energies in the desired range, we record the new offset energy as  $E_{i,\text{offset}} = E_{i,d} - E_i$  and use it in the next reinitialization process (after the next time step).

### G. Boundary conditions and contacts

As the simulation domain is finite, phonons might end up outside its boundaries. A phonon is reflected back inside if attempting to exit in the transverse (width) direction. A phonon exiting in the longitudinal direction is simply deleted.

As mentioned in Sec. II C, we keep a constant temperature at two ends of the ribbon with a “black-body cell” at each end.<sup>78</sup> After the drift and scattering processes, all the phonons inside these two end cells are deleted and replaced by a new cell ensemble according to the appropriate reservoir temperature, the same way as described in Sec. II C. This way all phonons coming out of the end cells are thermalized to the contact temperatures, and the two end cells act like black bodies.

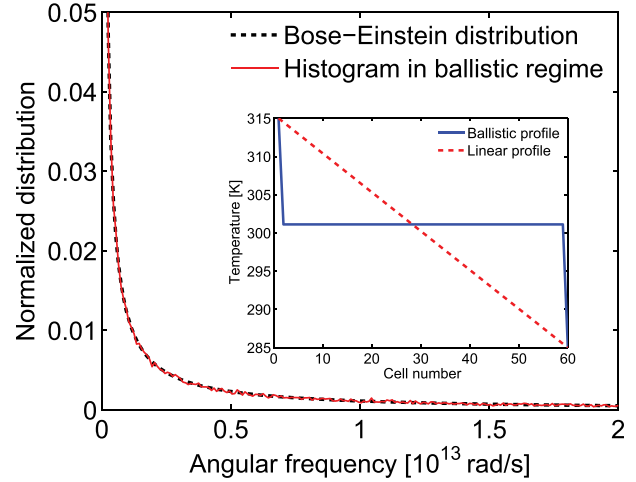


FIG. 8. (Main panel) Normalized phonon distribution histogram in the ballistic transport regime compared with the Bose-Einstein distribution. The histogram is obtained by running the simulation with all the scattering mechanism turned off and recording the energies of all the phonons inside the GNR after the steady state is established;  $T_h = 315$  K and  $T_c = 285$  K in this case. The Bose-Einstein distribution is obtained based on temperature  $T_{\text{ballistic}} = 301.12$  K inside the ribbon. (Inset) The calculated temperature profile inside the ribbon in the ballistic limit. The linear profile is also depicted for comparison.

## III. RESULTS AND DISCUSSION

### A. Temperature profile in the ballistic, quasiballistic, and diffusive limits

A good reliability test for PMC is a comparison between the simulation results and the diffusive and ballistic limits to the steady-state temperature profile. Purely diffusive transport should lead to a linear temperature profile, while ballistic transport would result in a constant temperature  $T_{\text{ballistic}} = \left(\frac{T_h^4 + T_c^4}{2}\right)^{1/4}$  inside the ribbon, with abrupt changes at the two ends.<sup>103</sup> For situations in between—the quasiballistic regime—the temperature profile is expected to have both features: a linear drop inside the ribbon, with abrupt changes at the two ends. We accurately capture all three regimes in the PMC simulation: calculations in the diffusive and

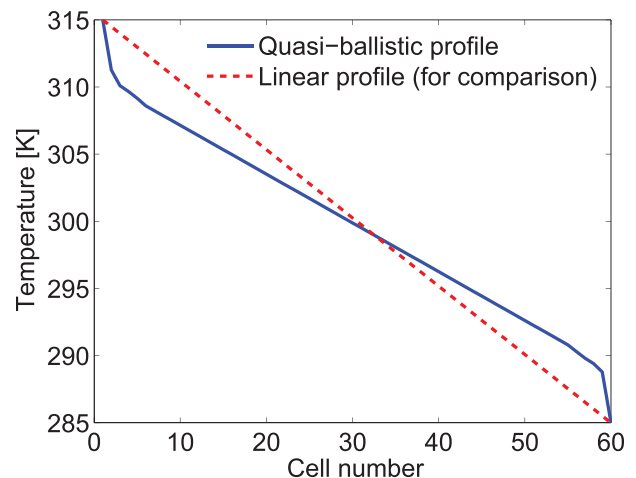


FIG. 9. A typical temperature profile along the ribbon in the quasiballistic transport regime. Here, the temperatures at two ends are  $T_h = 315$  K and  $T_c = 285$  K and the number of cells is  $N_c = 60$ .

ballistic limits are presented in the inset to Fig. 8, while the quasiballistic regime is depicted in Fig. 9.

Further, in order to validate our assumption of local equilibrium, especially in the ballistic regime, we made a phonon distribution histogram inside the ribbon in the steady state. The normalized histogram (main panel of Fig. 8) falls right on top of the theoretically calculated BE distribution, proving that our local equilibrium assumption stands even in the ballistic limit. Therefore, the PMC algorithm (Sec. II) is reliable from the ballistic all the way to the diffusive regime.

In the diffusive regime and under small temperature gradients, we can get the thermal conductivity from Fourier's law:  $\kappa = -\frac{\phi_a}{\nabla T}$ . In the quasiballistic regime, the gradient  $\nabla T$  is the slope of the linear region inside the ribbon (see Fig. 9).

## B. Thermal conductivity of wide GNRs: Comparison with experiment

We look at the thermal conductivity of graphene and GNRs from 300 K to 600 K, the range where most experiments are carried out.<sup>3,8,9,25,27,28,104–106</sup> Thermal conductivity of suspended GNRs generally depends on both width and length.<sup>9,27,29</sup> The width dependence comes from the relative importance of edge scattering to internal mechanisms; for wide enough GNRs, thermal conductivity no longer depends on the width.<sup>27,28</sup> To mimic transport in very wide GNRs, we use narrow rectangular ribbons whose edges are completely flat; flat edges ensure the lateral phonon velocity is conserved upon specular reflection, i.e., no backscattering occurs, and consequently there is no width dependence in their thermal conductivity.

Chen *et al.*<sup>9</sup> fabricated large-area graphene using the chemical vapor deposition (CVD) technique and transferred it onto a low-stress silicon-nitride-membrane substrate, with several holes of diameters  $D_h$  ranging from 3 to 10  $\mu\text{m}$ . Thereby, they obtained suspended circular graphene samples of given diameters and measured their thermal conductivities using Raman spectroscopy. There is no edge roughness and the characteristic length associated with the heat-flow direction is the hole diameter. We do not simulate circular samples here, but we can set the ribbon length  $L$  to match  $D_h$ , and the resulting thermal conductivity should be comparable to the experimental data.

In Fig. 10, we present the calculated thermal conductivity for GNRs with lengths comparable to the sample diameters in the experiments of Chen *et al.*<sup>9</sup> As the experiments were performed on CVD-grown, polycrystalline graphene, we have included grain-boundary scattering in the calculation. The simulation results agree well with the measurement from 300 K to 600 K and for various sizes. Based on our simulations, phonon transport in all these samples is still in the quasiballistic regime: the thermal conductivity monotonically increases with increasing sample length. Chen *et al.* observed a size dependence for samples from 3 to 8  $\mu\text{m}$ , but, owing to a large uncertainty in the measurements, they could not accurately extract a monotonic dependence over the size range. For the shortest (3  $\mu\text{m}$ , magenta curves) and longest (10  $\mu\text{m}$ , black curves) samples, we also compare the results with (solid lines) and without (dashed lines) grain boundary

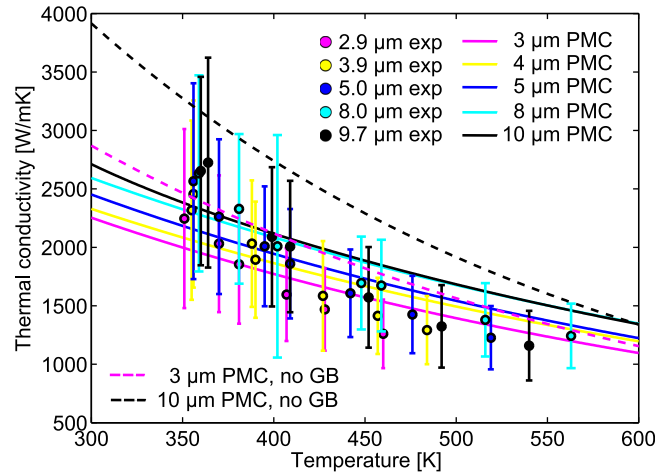


FIG. 10. Thermal conductivity of graphene for different lateral dimensions, as obtained by Chen *et al.*<sup>9</sup> in the circular geometry (symbols) and from our simulation in the rectangular GNR geometry with (solid lines) and without (dashed lines) grain boundary scattering.

scattering. The importance of grain boundary scattering decreases with increasing temperature, as the average mean free path (MFP) due to phonon-phonon scattering decreases and becomes comparable to a typical grain size. We note that the PMC results with grain boundary scattering included are in better agreement with experiment than the results without it. As these GNRs are in the quasiballistic regime, their thermal conductivity depends on length, the importance of grain boundary scattering is understandably more pronounced in longer GNRs.

## C. Thermal conductivity of wide GNRs: Ballistic-to-diffusive crossover

Length dependence of thermal conductivity comes from the relative magnitude of the phonon MFP  $\Lambda$  and the ribbon length  $L$ ; for long enough GNRs, transport would be diffusive and the length dependence would vanish. Ghosh *et al.*<sup>4</sup> estimated the MFP of graphene to be  $\Lambda \sim 800$  nm near room temperature. However, in our simulations, we find that  $\Lambda$  for

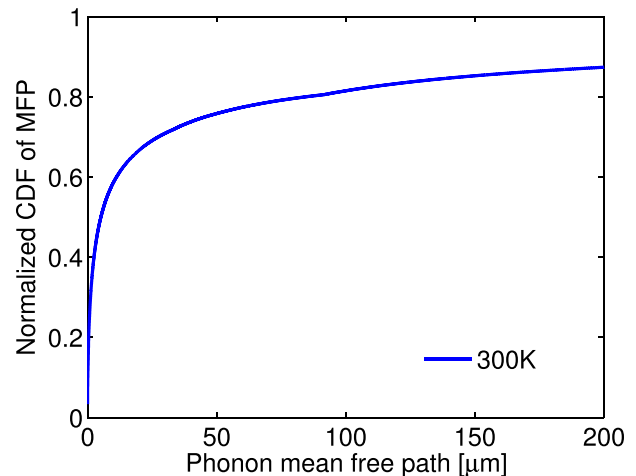


FIG. 11. Normalized cumulative distribution function of phonon mean free path for suspended graphene at 300 K. About 20% of phonons have a mean free path greater than 100  $\mu\text{m}$ .

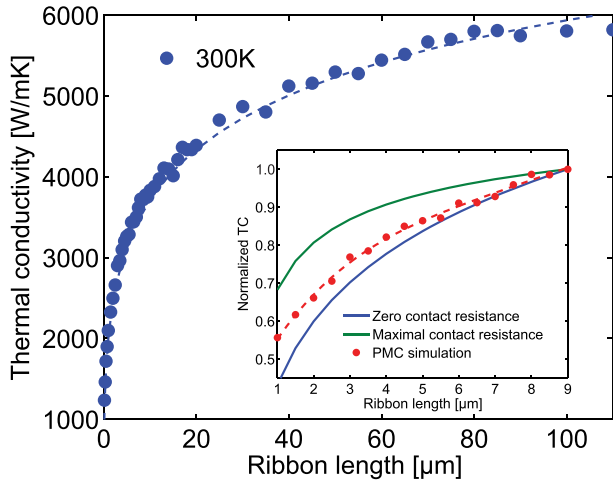


FIG. 12. Length-dependent thermal conductivity of wide GNRs at room temperature, obtained from the PMC simulation. Dashed line is a guide for the eye. (Inset) Comparison of normalized thermal conductivity from our simulation (red dots) and the experimentally obtained data of Xu *et al.*<sup>27</sup> The green curve shows the thermal conductivity estimated with maximal contact resistance, the blue one corresponds to the value with no contact resistance.

phonons in different branches and with different energies ranges from a few nanometers all the way up to hundreds of microns. Figure 11 shows the cumulative distribution function of the phonon mean free path  $\Lambda$  for suspended graphene at 300 K. Note that about 20% of phonons have  $\Lambda > 100 \mu\text{m}$  and more than 10% have  $\Lambda > 200 \mu\text{m}$ .

Figure 12 shows the calculated thermal conductivity of wide GNRs over a range of lengths  $L$  at room temperature. The thermal conductivity keeps increasing with increasing length up to  $L \sim 100 \mu\text{m}$ , which is to be expected considering that nearly 20% of phonons have a mean free path longer than that (see Fig. 11). This length is larger than any of the measured samples, therefore, all the existing experiments on suspended graphene<sup>3,8,9,27,104,105</sup> were carried out in the quasiballistic regime, so the maximal thermal conductivity of suspended bulk graphene could be higher than experimental reports indicate.

This simulation captures the ballistic-to-diffusive cross-over of phonon transport in suspended graphene.<sup>28</sup> In the purely ballistic transport regime, the thermal conductance  $G$  tends to a constant, while in the purely diffusive transport regime, the thermal conductivity  $\kappa$  is constant.  $G$  and  $\kappa$  are related through  $G = \kappa \frac{A}{L}$ , where  $A$  is the cross-sectional area perpendicular to the heat-flow direction and  $L$  is the length. We denote the constant thermal conductance in the ballistic regime as  $G_{\text{ball}}$  and the constant thermal conductivity in the diffusive regime as  $\kappa_{\text{diff}}$ . As  $L \rightarrow 0$ ,

$$\kappa \approx G_{\text{ball}} \cdot \frac{L}{A}. \quad (16a)$$

As  $L \rightarrow \infty$ , we have

$$\kappa \rightarrow \kappa_{\text{diff}}. \quad (16b)$$

At the left end of Fig. 12, thermal conductivity varies almost linearly with length, indicating ballistic transport.  $G_{\text{ball}}$  of GNR depends on width,<sup>107–109</sup> and from our simulation we

extract the room-temperature ballistic conductance per unit cross section as  $G_{\text{ball}}/A \approx 5 \times 10^9 \text{ W/m}^2\text{K}$ , which is close to the theoretical value of  $5.28 \times 10^9 \text{ W/m}^2\text{K}$  obtained by Muñoz, Lu, and Yakobson.<sup>108</sup> At the right end, thermal conductivity does saturate at very large lengths (around  $100 \mu\text{m}$  at room temperature). For the quasiballistic region in between, it is often assumed that the ballistic and diffusive transport channels can be connected “in series,” which would give  $\kappa^{-1} = \kappa_{\text{diff}}^{-1} + G_{\text{ball}}^{-1}A/L$ .<sup>28</sup> We find it impossible to fit the data using this expression; any such fit that is reasonable at low  $L$  drastically underestimates the diffusive limit. A dashed curve numerical fit in the main panel of Fig. 12, to guide the eye, follows  $\ln \kappa = 7.6 + 0.3 \ln L - 0.013 (\ln L)^2$ , i.e.,  $\kappa \approx 1998 L^{0.3} e^{-0.013 (\ln L)^2}$ . It is clear that this fit is poor in the diffusive limit, as it does not saturate, but may be appropriate for a number of experiments with GNRs shorter than  $100 \mu\text{m}$ .

Recently, Xu *et al.*<sup>27</sup> observed a length dependence of thermal conductivity in their suspended wide GNR samples. However, their measured thermal conductivity is much smaller than our simulation results as well as other experimental ones,<sup>9,25</sup> the offset is likely related to sample-preparation specifics. In order to compare with their length-dependence trend, we scaled their data and ours to 1 at the maximal length they measured. The inset to Fig. 12 shows a comparison between the scaled data from our PMC simulation and the experiment of Xu *et al.*<sup>27</sup> (experimental results are presented here via best quadratic fits to the data, green and blue curves). The blue line and the green line are the estimated maximal and minimal possible thermal conductivities, and our simulation falls right in between.

Furthermore, we calculated the diffusive-limit thermal conductivity  $\kappa_{\text{diff}}$  at different temperatures (Fig. 13). These indicate the upper limit thermal conductivity one can measure in graphene at various temperatures. As we have mentioned, almost all samples in experiments<sup>3,8,9,27,104,105</sup> are still in the quasiballistic regime, so  $\kappa_{\text{diff}}$  is higher than all experimental data. In Fig. 13, we show the comparison with predicted upper limit of thermal conductivity from Dorgan

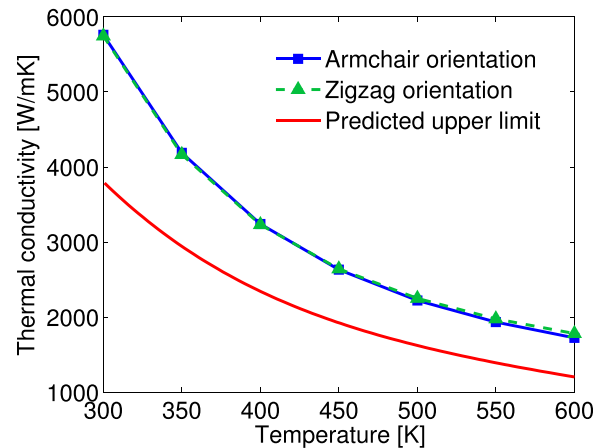


FIG. 13. Thermal conductivity for suspended pristine bulk graphene from the PMC simulation (squares—armchair direction, triangles—zigzag direction) and the maximal thermal conductivity predicted by Dorgan *et al.*<sup>55</sup>

*et al.*<sup>55</sup> We see that the difference reduces as the temperature increases, because the phonon MFP decreases as the temperature increases. As a result, for a given sample length, transport moves from quasiballistic to diffusive at higher temperatures; therefore, the measured values are closer to the calculated diffusive upper limit. Another insight we can take from Fig. 13 is that thermal transport is indeed isotropic for infinitely large graphene, which was predicted by first-principles calculations.<sup>110</sup>

#### D. Thermal conductivity of isotopically modified graphene

Thermal conductivity of graphene could be largely influenced by isotopes. Chen *et al.*<sup>25</sup> measured thermal conductivity of graphene with different <sup>13</sup>C compositions. From the simulation point of view, as the abundance of <sup>13</sup>C changes, phonon dispersion may slightly change because of the average atomic mass  $\bar{M}$ . Furthermore, the composition would change the rate of scattering from isotopes. For each <sup>13</sup>C composition measured in the experiment, we calculate the dispersion, PDOS, and group velocities in the same way as described in Sec. II A except with a different  $\bar{M}$ . The dimension of the ribbon is chosen as  $L = 2.8 \mu\text{m}$ , following experiment.<sup>25</sup>

Figure 14 shows the temperature dependence for four different compositions from experiment<sup>25</sup> compared with our PMC simulation results. We are able to capture the composition-dependence trend: thermal conductivity with 50% <sup>13</sup>C is the lowest because the two isotopes are equally mixed, giving rise to maximal isotope scattering. In general, our simulation data agree well with experiment in a large temperature and <sup>13</sup>C abundance range.

Figure 15 shows a direct comparison of thermal conductivity versus <sup>13</sup>C composition at a fixed temperature ( $T = 380 \text{ K}$ ). Our results are within the measured range and are even closer to the experimental data than the molecular dynamics simulation results reported by Chen *et al.* themselves.<sup>25</sup>

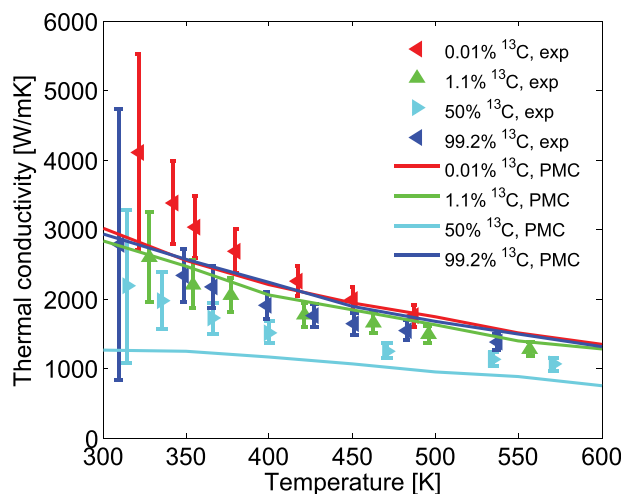


FIG. 14. Thermal conductivity of graphene with different <sup>13</sup>C abundance as a function of temperature. Symbols represent the experimental data from Chen *et al.*<sup>9</sup> and lines show our PMC simulation results.

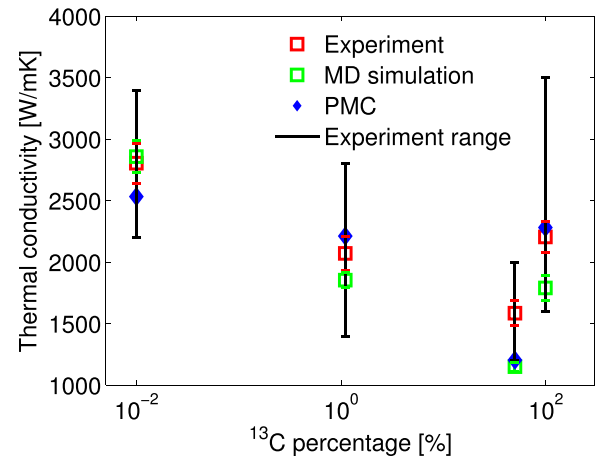


FIG. 15. Thermal conductivity of graphene as a function of <sup>13</sup>C abundance at 380 K. Red squares show the experimental data from Chen *et al.*<sup>25</sup> green squares are the MD simulation results from the same paper, and blue diamonds correspond to the PMC simulation.

#### E. Thermal conductivity of GNRs with edges: Width dependence

We simulated thermal transport in AGNRs and ZGNRs, assuming perfect armchair and zigzag edges, with each segment in the edge structure having the length of the graphene C-C bond in equilibrium. Perfectly periodic edge structures have been achieved in practice for both armchair<sup>15,19,111,112</sup> and zigzag<sup>15,111,112</sup> orientations. Both theoretical<sup>113</sup> and experimental<sup>114</sup> works show the perfect armchair edge to be stable. The zigzag edge is relatively stable, though theory predicts that the zigzag edge can reconstruct to a pentagon-heptagon shape and become more stable.<sup>113</sup> Experiments showed that reconstructions in both directions (from all hexagon to pentagon-heptagon and from pentagon-heptagon to all hexagon) are spontaneous under the experimental environment conditions.<sup>114</sup> It was also shown that the bond length and angle between bonds at the edges may differ slightly from those inside the ribbon.<sup>113,114</sup>

In the PMC simulation with full dispersion, we need the edge structure sharing the symmetry of the lattice (see

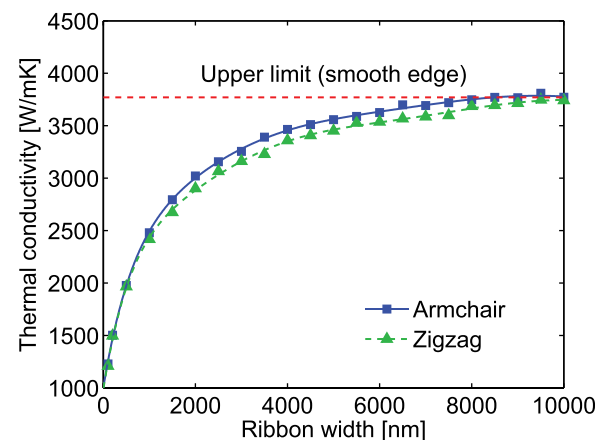


FIG. 16. Thermal conductivity of  $10 \mu\text{m}$ -long AGNRs (blue squares) and ZGNRs (green triangles) at 300 K as a function of GNR width, obtained from the PMC simulation. The red dashed line is the upper limit of thermal conductivity for the same length, calculated with a flat-edge GNR.

Sec. II D) in order to conserve the phonon distribution upon specular reflections from the edge, so we work with perfect armchair and zigzag edges. For simplicity, we use the equilibrium bond length as the length of our edge segments and neglect the bond-angle changes.

Figure 16 shows the width dependence of thermal conductivity for both AGNRs and ZGNRs at 300 K. We see that the thermal conductivity for both orientations varies greatly with width, approaching the smooth-edge value for the same length in the wide-GNR limit. The difference with respect to orientation is minute and is within the PMC error.

### F. Full-dispersion vs isotropic-dispersion PMC

Finally, we address the question how important it is to account for full phonon dispersions in the PMC simulation of transport in GNRs, as this aspect adds to computational complexity. To that end, we considered thermal transport in GNRs of length  $L = 10 \mu\text{m}$  but with different widths and orientations. Figure 17 shows the calculated thermal conductivity as a function of temperature for 500-nm, 200-nm, and 100-nm wide GNRs. For each width, we considered an AGNR and a ZGNR with appropriate edges and full phonon dispersions, and an AGNR with isotropic dispersions. For each acoustic branch, the isotropic dispersion approximation was obtained from a quadratic fit to the full dispersion,  $\omega_b = v_{s,b}q + c_b q^2$ . Here,  $c_{TA} = -1.15 \times 10^{-7}$ ,  $c_{LA} = -3.95 \times 10^{-7}$ , and  $c_{ZA} = 2.83 \times 10^{-7}$  (in  $\text{m}^2/\text{s}$ ), while  $v_{s,TA} = 1.17 \times 10^4$ ,  $v_{s,LA} = 2.19 \times 10^4$ , and  $v_{s,ZA} = 2.28 \times 10^3$  (in  $\text{m/s}$ ).

Based on Fig. 17, we see that the isotropic dispersion approximation generally overestimates thermal conductivity, quite dramatically so at low temperatures. The relative error brought about by the use of isotropic approximation at low temperatures is quite high in narrow GNRs, where edge roughness dominates. The difference between full and isotropic dispersions decreases with increasing temperature. The trend is intuitively plausible, as orientation-dependent edge-roughness scattering dominates at low temperatures, while the momentum-randomizing three-phonon scattering takes over

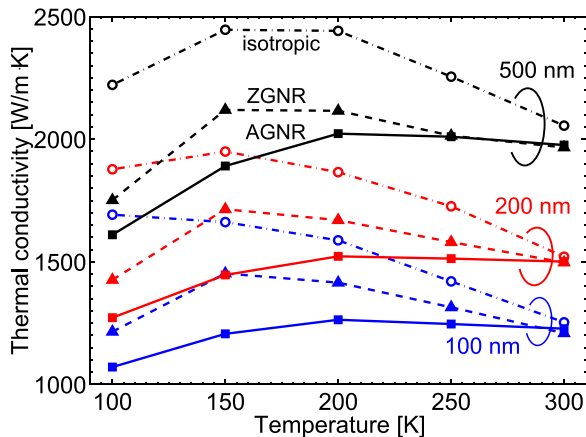


FIG. 17. Thermal conductivity versus temperature for GNRs of width 500 nm (black), 200 nm (red), and 100 nm (blue) calculated based on PMC. For each width, we present data obtained with isotropic dispersion (open circles), as well as with full dispersion assuming the AGNR (solid squares) and ZGNR (solid triangles) ribbon orientation.

as the temperature increases. We also note that the thermal conductivity of ZGNRs is higher than that of AGNRs, in agreement with the results of atomistic studies.<sup>34,40,50,115</sup>

### IV. CONCLUSION

We studied phonon transport in suspended single-layer graphene and micron-sized GNRs using the full-dispersion PMC technique. The calculated thermal conductivity is in good agreement with experimental measurements of Chen *et al.*<sup>9,25</sup> and Xu *et al.*<sup>27</sup> We captured the ballistic-to-diffusive crossover in thermal conductivity and found that the diffusive limit at room temperature is not reached in most experiments, as lengths over  $100 \mu\text{m}$  are needed. Consequently, the diffusive upper limit is likely higher than predicted,<sup>55</sup> and we calculate it for temperatures up to 600 K. We show that the GNR orientation matters for thermal transport, with ZGNRs having higher thermal conductivity than AGNRs in micron-sized systems, which is the same trend observed in atomistic calculations. The error made by employing the isotropic dispersion approximation for transport in GNRs is not large at room temperature, but the results with isotropic dispersions generally overestimate thermal conductivity and quite considerably so at low temperatures and in narrow GNRs.

The full-dispersion PMC technique, presented here in detail, combines an efficient transport kernel (including inelastic and elastic scattering, as well as enabling the incorporation of real-space edge features) with an accurate account of phonon dispersions. This technique is a good choice—in terms of accuracy, computational efficiency, and adaptability to different materials or geometries—for analyzing systems with pronounced directional sensitivity (such as GNRs, or generally semiconductor membranes and nanowires), which have rough boundaries and are too large to address using atomistic techniques.

### ACKNOWLEDGMENTS

This work was supported by the NSF under Award No. 1201311 (S.M.) and by the U.S. Department of Energy, Office of Basic Energy Sciences, Division of Materials Sciences and Engineering under Award No. DE-SC0008712 (L.N.M. and I.K.). The simulation work was performed using the computer resources and assistance of the UW-Madison Center For High Throughput Computing (CHTC) in the Department of Computer Sciences. The CHTC is supported by UW-Madison and the Wisconsin Alumni Research Foundation, and is an active member of the Open Science Grid, which is supported by the National Science Foundation and the U.S. Department of Energy's Office of Science.

### APPENDIX A: ALGORITHM FOR FINDING THE WAVE VECTOR

The second main step in single phonon generation (Sec. II C 2) is using the rejection technique to find an appropriate wave vector  $\mathbf{q}$  for a phonon with energy  $\hbar\omega$  and in branch  $b$ . Figure 18 shows a set of isoenergy curves (separated by  $2 \times 10^{13}$  rad/s) for the TA mode (the other two modes have

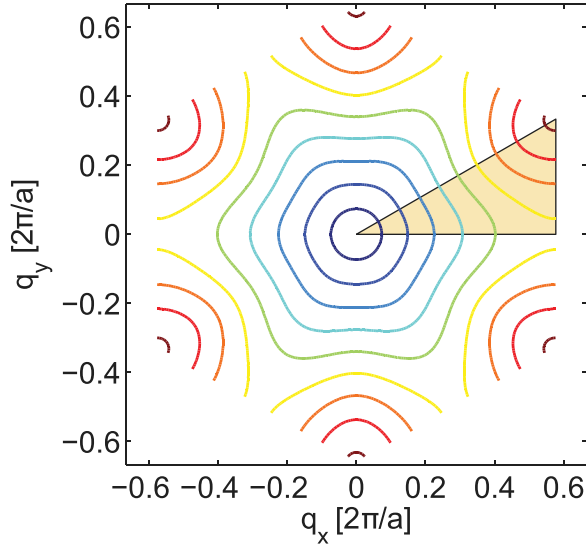


FIG. 18. Isoenergy curves in the 1BZ for TA-branch phonons. The neighboring curves are separated by  $2 \times 10^{13}$  rad/s and the shaded region in the black triangle is the irreducible wedge in the 1BZ.

similar curves). As we can see, the curves have near-radial symmetry, thus we use polar coordinates for convenience. If we know the phonon frequency and branch, we have already fixed the isoenergy curve and only an angle  $\theta$  is needed to uniquely find a point on it. Further, the 1BZ has 12-fold symmetry following the graphene lattice, so we would only need to consider the irreducible wedge (shaded area in Fig. 18), and map it onto any one of its counterparts with equal probability. Evaluating the probability of a phonon having angle  $\theta$  on a particular isoenergy curve  $\omega$  is like a discretized version of PDOS calculation in Sec. II A. The probability is represented by

$$p(\omega, \theta) \propto \frac{\text{arc}(\theta - \delta\theta, \theta + \delta\theta)}{|\mathbf{v}_g(\omega, \theta)|}, \quad (\text{A1})$$

where  $\text{arc}(\theta - \delta\theta, \theta + \delta\theta)$  is the arc length on the isoenergy curve between  $(\theta - \delta\theta, \theta + \delta\theta)$  and  $|\mathbf{v}_g(\omega, \theta)|$  is the magnitude of group velocity (we assume the group velocity is constant along the small arc). To make a rejection table, we need to discretize both the angular frequency and the angle in irreducible wedge. For the frequency, we still use the same discretization as in Sec. II A. For the angle, we divide the central angle of the irreducible wedge ( $\theta_{\max} = \frac{\pi}{6}$ ) into  $N_a$  equal intervals with  $\Delta\theta = \frac{\theta_{\max}}{N_a}$ . The central frequency in the  $i$ th interval is  $\theta_{c,i} = (2i - 1)\frac{\Delta\theta}{2}$ . We evaluate (A1) only at discrete points  $(\omega_{c,i}, \theta_{c,j})$  and get a  $N_{\text{int}} \times N_a$  interpolation table. For any  $0 < \omega < \omega_{\max}$  and  $0 < \theta < \theta_{\max}$ , we can get the probability of having a phonon from interpolation. We find that  $N_a = 100$  serves the purpose of accurate interpolation.

Another effect caused by the full dispersion is that the group velocity at which phonons travel is no longer parallel to their wave vectors. So we need to find not only the proper wave vector but also the associated group velocity. In practice, we do not use the wave vector in the simulation and it only serves as a bridge to connect the dispersion and the phonon velocity. As we have mentioned, for each chosen  $(\omega, \theta)$

pair in branch b, there is only one unique point in the dispersion curve. As a result, for each of the  $N_{\text{int}} \times N_a$  discrete points  $(\omega_{c,i}, \theta_{c,j})$  we evaluated the probability, we can find a unique point on dispersion curve and evaluate the group velocity  $\mathbf{v}_g(\omega_{c,i}, \theta_{c,j})$ . Since the group velocity is a vector, we actually get two tables,  $v_x(\omega_{c,i}, \theta_{c,j})$  and  $v_y(\omega_{c,i}, \theta_{c,j})$ . Figure 19 shows a point and its associated  $\mathbf{q}$  and  $\mathbf{V}_g$ . The shaded area shows the irreducible wedge. We now have all the tables we need for phonon generation: the probability table  $p(\omega_{c,i}, \theta_{c,j})$  and the two components of group velocity table  $v_x(\omega_{c,i}, \theta_{c,j})$  and  $v_y(\omega_{c,i}, \theta_{c,j})$ . We need a set of these tables for each branch, and that makes  $3 \times 3 = 9$  tables in total. All the tables are  $N_{\text{int}} \times N_a$  (in our case  $2500 \times 100$ ) in size and are pre-calculated and recorded before the actual simulation.

From previous steps, we have already chosen the angular frequency  $\omega$  and the branch b for our phonon. The first thing to do now is to interpolate in each of the three 2D tables for branch b and get three 1D tables associated with our specified frequency level  $\omega$ . The interpolation for the three tables is the same and we would take the probability table  $p(\omega_{c,i}, \theta_{c,j})$  as an example. With simple algebra, we can find the index  $m$  satisfying  $\omega_{c,m} < \omega < \omega_{c,m+1}$ . Then, we get the probability of finding a phonon with angle  $\theta_{c,j}$  at level  $\omega$  from weighted average of  $p(\omega_{c,m}, \theta_{c,j})$  and  $p(\omega_{c,m+1}, \theta_{c,j})$ .

$$p(\theta_{c,j})|_{\omega} = p(\omega_{c,m}, \theta_{c,j}) \cdot (1 - d) + p(\omega_{c,m+1}, \theta_{c,j}) \cdot d, \quad (\text{A2})$$

$$j = 1 \dots N_a,$$

where the weighting factor is  $d = \frac{\omega - \omega_{c,m}}{\Delta\omega}$ . Now we can normalize this 1D probability table so that the maximal value in the table is unity. Note that we can only normalize the probability table after interpolation between frequency levels. We still call the normalized table  $p(\theta_{c,j})|_{\omega}$ . For the velocities, we get  $v_x(\theta_{c,j})|_{\omega}$  and  $v_y(\theta_{c,j})|_{\omega}$  tables in the same way except that we do not normalize them. Now we are working only on the frequency level  $\omega$ , so we omit the subscript  $\omega$  and just call the tables  $p(\theta_{c,j})$ ,  $v_x(\theta_{c,j})$  and  $v_y(\theta_{c,j})$  from now on for brevity.

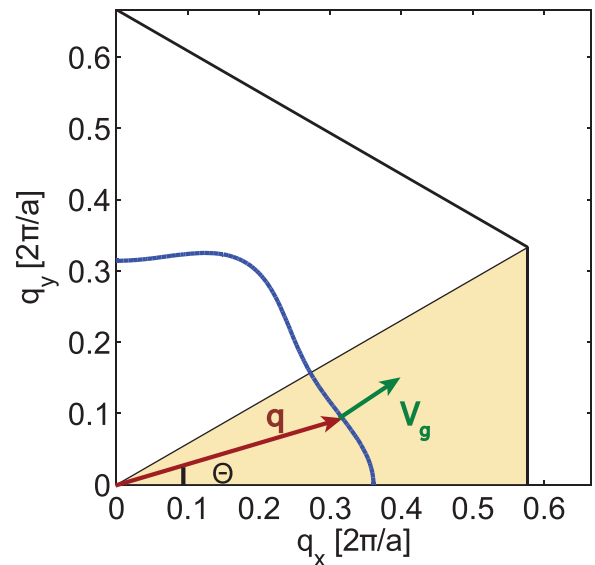


FIG. 19. A typical isoenergy curve ( $\omega = 9 \times 10^{13}$  rad/s). The shaded area shows the irreducible wedge. Angle  $\theta$  fixes a point at the curve and the associated wave vector  $\mathbf{q}$  and group velocity  $\mathbf{v}_g$  are shown.

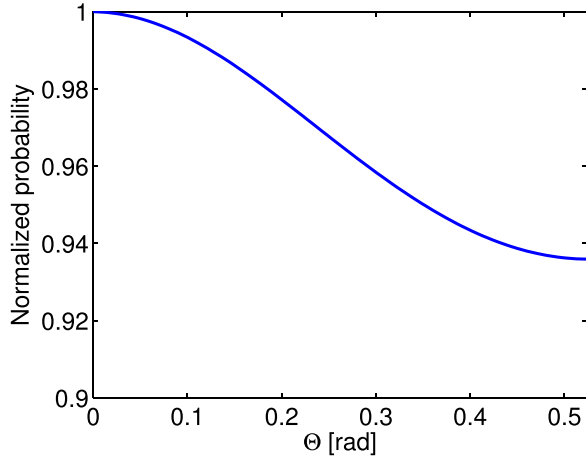


FIG. 20. A typical normalized probability versus angle curve for phonon generation. Here, the frequency level is at  $\omega = 3 \times 10^{13}$  rad/s in TA-branch.

Next, we use the rejection technique to choose a point on the dispersion curve. For a typical  $\omega$  value, the probability table looks like Fig. 20 (the figure shows the table for frequency level  $\omega = 3 \times 10^{13}$  rad/s in TA-branch). Draw a pair of random numbers  $(x, y)$ . We would use  $x$  to get the angle and compare  $y$  with the probability to decide whether we accept the angle or not. The chosen angle is  $\theta = x \cdot \theta_{\max}$ , where  $\theta_{\max}$  is the maximal central angle in the irreducible 1BZ as we have mentioned before. We need to compare  $y$  to  $p(\theta)$  and the probability is again obtained from interpolation. Seek the index  $n$  satisfying  $\theta_n < \theta < \theta_{n+1}$  and similarly,

$$p(\theta) = p(\theta_n) \cdot (1 - d') + p(\theta_{n+1}) \cdot d', \quad (\text{A3})$$

where  $d' = \frac{\theta - \theta_n}{\Delta\theta}$  is the weighting factor. If  $y < p(\theta)$ , then the angle is accepted and a point has been uniquely chosen in the irreducible wedge. We can then use the  $v_x(\theta_{c,j})$  and  $v_y(\theta_{c,j})$  tables to get the group velocity  $v_x$  and  $v_y$  for the phonon at this point. Otherwise, the angle should be rejected, and we keep drawing random number pairs  $(x, y)$  until one angle is accepted.

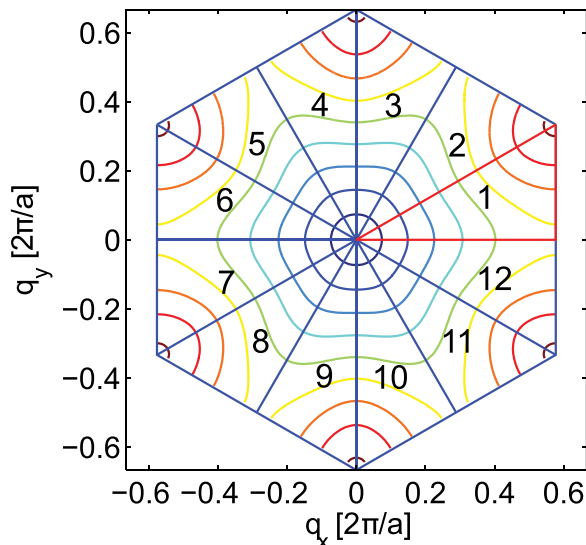


FIG. 21. Twelve equivalent triangles in 1BZ numbered clockwise.

TABLE II. Mapping rule of calculating the final group velocities  $v_x^{\text{final}}$  and  $v_y^{\text{final}}$  from the group velocities  $v_x$  and  $v_y$  in the irreducible wedge of the 1BZ according to the triangle index.

Index	1	2	3
$v_x^{\text{final}}$	$v_x$	$\frac{1}{2}v_x + \frac{\sqrt{3}}{2}v_y$	$\frac{1}{2}v_x - \frac{\sqrt{3}}{2}v_y$
$v_y^{\text{final}}$	$v_y$	$\frac{\sqrt{3}}{2}v_x - \frac{1}{2}v_y$	$\frac{\sqrt{3}}{2}v_x + \frac{1}{2}v_y$
Index	4	5	6
$v_x^{\text{final}}$	$-\frac{1}{2}v_x + \frac{\sqrt{3}}{2}v_y$	$-\frac{1}{2}v_x - \frac{\sqrt{3}}{2}v_y$	$-v_x$
$v_y^{\text{final}}$	$\frac{\sqrt{3}}{2}v_x + \frac{1}{2}v_y$	$\frac{\sqrt{3}}{2}v_x - \frac{1}{2}v_y$	$v_y$
Index	7	8	9
$v_x^{\text{final}}$	$-v_x$	$-\frac{1}{2}v_x - \frac{\sqrt{3}}{2}v_y$	$-\frac{1}{2}v_x + \frac{\sqrt{3}}{2}v_y$
$v_y^{\text{final}}$	$-v_y$	$-\frac{\sqrt{3}}{2}v_x + \frac{1}{2}v_y$	$-\frac{\sqrt{3}}{2}v_x - \frac{1}{2}v_y$
Index	10	11	12
$v_x^{\text{final}}$	$\frac{1}{2}v_x - \frac{\sqrt{3}}{2}v_y$	$\frac{1}{2}v_x + \frac{\sqrt{3}}{2}v_y$	$v_x$
$v_y^{\text{final}}$	$-\frac{\sqrt{3}}{2}v_x - \frac{1}{2}v_y$	$\frac{\sqrt{3}}{2}v_x - \frac{1}{2}v_y$	$-v_y$

The last step in phonon generation is to map the point we found in irreducible 1BZ to the whole 1BZ and modify the group velocity accordingly. The 12 equivalent triangles in 1BZ are shown in Fig. 21 and we number them clockwise. A random number  $R_4$  is used to choose one of the triangles and the index of the chosen triangle is ceiling  $(12 \times R_4)$ . Then, the final group velocities  $v_x^{\text{final}}$  and  $v_y^{\text{final}}$  can be obtained from  $v_x$  and  $v_y$  by simple combinations of rotation and flipping according to the symmetry. The mapping rules are shown in Table II. After the mapping, we finally have a phonon satisfying all the distribution requirements and we can add this phonon to a random position in its cell.

Finally, GNRs could have different orientations, with the armchair (AGNR) and zigzag (ZGNR) nanoribbon orientations being highly symmetric (Fig. 4). The presentation thus far applies to phonon in AGNRs. The only modification needed to simulate the transport in other orientations is to rotate  $v_g$  with the angle  $\Theta_o$  between the armchair orientation and the simulated orientation in phonon generation process. In particular, for ZGNRs, the rotation angle is  $\Theta_o = \frac{\pi}{6}$ .

## APPENDIX B: SCATTERING MECHANISMS

### 1. Phonon-phonon scattering

Phonon-phonon scattering dominates in the temperature range of our interest (300–600 K) for suspended graphene. Three-phonon interactions are very important for thermal conductivity calculation.<sup>29,116</sup> Three-phonon processes consist of two types: the normal (N) processes conserve both energy and momentum explicitly, while the umklapp (U) processes conserve energy but only conserve momentum up to a reciprocal lattice vector. Therefore, N processes do not directly cause thermal resistance but play a role through redistributing phonons. In principle, we could consider the 3-phonon interactions explicitly in the drift process when phonons come close, but that would be computationally very expensive and the accuracy still depends on how often we check the positions and the resolution of the dispersion. Therefore, we treat the 3-phonon interactions through a scattering rate like previous work.<sup>71,78,90</sup> For graphene, the three-phonon scattering rate is written as<sup>29</sup>

$$\tau_{b,U}^{-1}(\omega) = \frac{\hbar\gamma_b^2}{M\Theta_b v_{s,b}^2} \omega^2 T e^{-\Theta_b/3T}. \quad (\text{B1})$$

Here, as in Sec. III F,  $v_{s,b}$  is the mode-dependent sound velocity, which is determined from the average slope of the dispersion curve near the  $\Gamma$  point ( $v_{s,TA} = 1.17 \times 10^4$  m/s,  $v_{s,LA} = 2.19 \times 10^4$  m/s, and  $v_{s,ZA} = 2.28 \times 10^3$  m/s).  $\bar{M}$  is the average atomic mass in graphene and  $\Theta_b$  is the mode-specific Debye temperature obtained from

$$\Theta_b^2 = \frac{5\hbar^2}{3k_B^2} \frac{\int \omega^2 D_b(\omega) d\omega}{\int D_b(\omega) d\omega}. \quad (\text{B2})$$

In our case, (B2) is numerically evaluated and the Debye temperature for three branches is  $\Theta_{TA} = 1126.18$  K,  $\Theta_{LA} = 1826.39$  K, and  $\Theta_{ZA} = 623.62$  K, respectively. The strength of the scattering process is also controlled by the Grüneisen parameter  $\gamma_b$ , here we take  $\gamma_{LA} = 2$ ,  $\gamma_{TA} = \frac{2}{3}$ , and  $\gamma_{ZA} = -1.5$ .<sup>29</sup> The first half of the rate is the standard Umklapp interaction strength,<sup>116</sup> and the exponential term adds the effective contribution from the redistribution via the N processes.

## 2. Isotope scattering

Though pristine graphene does not have impurities, phonons could still scatter from the mass difference due to the naturally present isotopes. For carbon, the natural abundance is 98.9% for <sup>12</sup>C and 1.1% for <sup>13</sup>C. The mode-dependent isotope scattering rate is<sup>70</sup>

$$\tau_{b,I}^{-1}(\omega) = \frac{\pi}{2} \Gamma \Omega_0 \omega^2 D_b(\omega), \quad (\text{B3})$$

where

$$\Gamma = \sum_i f_i (1 - M_i/\bar{M})^2 \quad (\text{B4})$$

is the mass difference constant and  $f_i$  is the abundance of the  $i$ th isotope and  $\Omega_0 \approx 2.62 \times 10^{-20}$  m<sup>2</sup> is the average area occupied by one carbon atom. In our simulation, we consider both natural abundance and the isotopically modified graphene samples. As a matter of fact, from Eq. (3) we know that atom mass enters the equation of motion, therefore, the percentage of isotopes would also slightly modify the dispersion relation through the average atomic mass  $\bar{M}$ . Since the change of  $\bar{M}$  is not large (varying from 12 to 13), the general shape of dispersion is the same and only the group velocities slightly change. But we use the modified dispersion to generate tables for more accuracy. Isotope scattering is an elastic process, so when a phonon is scattered by the isotope, we keep the phonon mode and angular frequency  $\omega$ , then randomly find a new wave vector/group velocity for it with respect to the phonon dispersion relation.

## 3. Grain boundary scattering

Single-crystal graphene samples are obtained through exfoliation, which is not scalable. Chemical vapor deposition on transition metal substrates such as copper has been used to synthesize good-quality large-area graphene,<sup>117</sup> yet CVD-fabricated graphene is always polycrystalline so phonons

scatter from the grain boundaries, which yield as extra resistance. The expression for the grain-boundary scattering rate<sup>118</sup> is

$$\tau_{GB}^{-1} = \frac{v}{l_G} \Xi(\omega), \quad (\text{B5})$$

inversely proportional to the average grain size  $l_G$ .  $\Xi(\omega) = \frac{1}{t_{GB}(\omega)} - 1$  describes the influence of transmission coefficient  $t_{GB}(\omega)$  at the boundary. This matters because when a phonon hits the grain boundary, it could either transmit as if nothing was there or be reflected, and the probability of transmission is dependent on the energy, represented by  $t_{GB}(\omega)$ . One can get the transmission coefficient from first principle calculations, but usually, for simplicity, we ignore the  $\omega$  dependence of the transmission, and  $\Xi(\omega)$  reduces to a coefficient describing the influence of the average transmission. We treat the grain boundary scattering as an elastic scattering process just like isotope scattering. Another reason why we could ignore the  $\omega$  dependence is that, with the CVD technique, the average grain size in polycrystalline graphene could be quite large and the grain boundary scattering rate is fairly small compared to other intrinsic scattering events. This is also why CVD graphene shares a lot of extraordinary properties of exfoliated graphene in experiment.<sup>119–121</sup> A recent account of phonon transport in polycrystalline suspended graphene, considering the grain-size distribution, can be found in Ref. 65.

<sup>1</sup>K. S. Novoselov, A. K. Geim, S. V. Morozov, D. Jiang, M. I. Katsnelson, I. V. Grigorieva, S. V. Dubonos, and A. A. Firsov, *Nature* **438**, 197 (2005).

<sup>2</sup>Y. Zhang, Y.-W. Tan, H. L. Stormer, and P. Kim, *Nature* **438**, 201 (2005).

<sup>3</sup>A. A. Balandin, S. Ghosh, W. Bao, I. Calizo, D. Teweldebrhan, F. Miao, and C. N. Lau, *Nano Lett.* **8**, 902 (2008).

<sup>4</sup>S. Ghosh, I. Calizo, D. Teweldebrhan, E. P. Pokatilov, D. L. Nika, A. A. Balandin, W. Bao, F. Miao, and C. N. Lau, *Appl. Phys. Lett.* **92**, 151911 (2008).

<sup>5</sup>R. Prasher, *Science* **328**, 185 (2010).

<sup>6</sup>I. W. Frank, D. M. Tanenbaum, A. M. van der Zande, and P. L. McEuen, *J. Vac. Sci. Technol., B* **25**, 2558 (2007).

<sup>7</sup>C. Lee, X. Wei, J. W. Kysar, and J. Hone, *Science* **321**, 385 (2008).

<sup>8</sup>J.-U. Lee, D. Yoon, H. Kim, S. W. Lee, and H. Cheong, *Phys. Rev. B* **83**, 081419 (2011).

<sup>9</sup>S. Chen, A. L. Moore, W. Cai, J. W. Suk, J. An, C. Mishra, C. Amos, C. W. Magnuson, J. Kang, L. Shi, and R. S. Ruoff, *ACS Nano* **5**, 321 (2011).

<sup>10</sup>D. L. Nika, S. Ghosh, E. P. Pokatilov, and A. A. Balandin, *Appl. Phys. Lett.* **94**, 203103 (2009).

<sup>11</sup>G. A. Slack, *J. Appl. Phys.* **35**, 3460 (1964).

<sup>12</sup>E. Pop, V. Varshney, and A. K. Roy, *MRS Bull.* **37**, 1273 (2012).

<sup>13</sup>K. A. Ritter and J. W. Lyding, *Nature Mater.* **8**, 235 (2009).

<sup>14</sup>W. Liu, B. L. Jackson, J. Zhu, C. Q. Miaou, C.-H. Chung, Y. J. Park, K. Sun, J. Woo, and Y.-H. Xie, *ACS Nano* **4**, 3927 (2010).

<sup>15</sup>X. Li, X. Wang, L. Zhang, S. Lee, and H. Dai, *Science* **319**, 1229 (2008).

<sup>16</sup>S. Datta, D. Strachan, S. Khamis, and A. Johnson, *Nano Lett.* **8**, 1912 (2008).

<sup>17</sup>L. Jiao, L. Zhang, X. Wang, G. Diankov, and H. Dai, *Nature* **458**, 877 (2009).

<sup>18</sup>D. V. Kosynkin, A. L. Higginbotham, A. Sinitskii, J. R. Lomeda, A. Dimiev, B. K. Price, and J. M. Tour, *Nature* **458**, 872 (2009).

<sup>19</sup>J. Cai, P. Ruffieux, R. Jaafar, M. Bieri, T. Braun, S. Blankenburg, M. Muoth, A. P. Seitsonen, M. Saleh, X. Feng, K. Müllen, and R. Fasel, *Nature* **466**, 470 (2010).

<sup>20</sup>M. Sprinkle, M. Ruan, Y. Hu, J. Hankinson, M. Rubio-Roy, B. Zhang, X. Wu, C. Berger, and W. A. de Heer, *Nat. Nanotechnol.* **5**, 727 (2010).

- <sup>21</sup>J. G. Son, M. Son, K.-J. Moon, B. H. Lee, J.-M. Myoung, M. S. Strano, M.-H. Ham, and C. A. Ross, *Adv. Mater.* **25**, 4723 (2013).
- <sup>22</sup>A. N. Abbas, G. Liu, B. Liu, L. Zhang, H. Liu, D. Ohlberg, W. Wu, and C. Zhou, *ACS Nano* **8**, 1538 (2014).
- <sup>23</sup>D. L. Nika and A. A. Balandin, *J. Phys.: Condens. Matter* **24**, 233203 (2012).
- <sup>24</sup>J. H. Seol, I. Jo, A. L. Moore, L. Lindsay, Z. H. Aitken, M. T. Pettes, X. Li, Z. Yao, R. Huang, D. Broido, N. Mingo, R. S. Ruoff, and L. Shi, *Science* **328**, 213 (2010).
- <sup>25</sup>S. Chen, Q. Wu, C. Mishra, J. Kang, H. Zhang, K. Cho, W. Cai, A. A. Balandin, and R. S. Ruoff, *Nature Mater.* **11**, 203 (2012).
- <sup>26</sup>A. A. Balandin and D. L. Nika, *Mater. Today* **15**, 266 (2012).
- <sup>27</sup>X. Xu, L. F. C. Pereira, Y. Wang, J. Wu, K. Zhang, X. Zhao, S. Bae, C. Tinh Bui, R. Xie, J. T. L. Thong, B. H. Hong, K. P. Loh, D. Donadio, B. Li, and B. Ozyilmaz, *Nat. Commun.* **5**, 3689 (2014).
- <sup>28</sup>M.-H. Bae, Z. Li, Z. Aksamija, P. N. Martin, F. Xiong, Z.-Y. Ong, I. Knezevic, and E. Pop, *Nat. Commun.* **4**, 1734 (2013).
- <sup>29</sup>Z. Aksamija and I. Knezevic, *Appl. Phys. Lett.* **98**, 141919 (2011).
- <sup>30</sup>Z. Aksamija and I. Knezevic, *Phys. Rev. B* **86**, 165426 (2012).
- <sup>31</sup>D. Nika, E. Pokatilov, A. Askerov, and A. Balandin, *Phys. Rev. B* **79**, 155413 (2009).
- <sup>32</sup>W. Zhang, T. S. Fisher, and N. Mingo, *Numer. Heat Transfer, Part B* **51**, 333 (2007).
- <sup>33</sup>J.-S. Wang, B. Agarwalla, H. Li, and J. Thingna, *Front. Phys.* (published online).
- <sup>34</sup>Y. Xu, X. Chen, B.-L. Gu, and W. Duan, *Appl. Phys. Lett.* **95**, 233116 (2009).
- <sup>35</sup>Y. Xu, X. Chen, J.-S. Wang, B.-L. Gu, and W. Duan, *Phys. Rev. B* **81**, 195425 (2010).
- <sup>36</sup>H. Sevinçli and G. Cuniberti, *Phys. Rev. B* **81**, 113401 (2010).
- <sup>37</sup>Z. Huang, T. S. Fisher, and J. Y. Murthy, *J. Appl. Phys.* **108**, 094319 (2010).
- <sup>38</sup>J.-W. Jiang, B.-S. Wang, and J.-S. Wang, *Appl. Phys. Lett.* **98**, 113114 (2011).
- <sup>39</sup>Z.-X. Xie, K.-Q. Chen, and W. Duan, *J. Phys.: Condens. Matter* **23**, 315302 (2011).
- <sup>40</sup>Z. W. Tan, J.-S. Wang, and C. K. Gan, *Nano Lett.* **11**, 214 (2011).
- <sup>41</sup>P. Scuracchio, S. Costamagna, F. M. Peeters, and A. Dobry, *Phys. Rev. B* **90**, 035429 (2014).
- <sup>42</sup>J. Lan, Y. Cai, G. Zhang, J.-S. Wang, and Y.-W. Zhang, *J. Phys. D: Appl. Phys.* **47**, 265303 (2014).
- <sup>43</sup>H. Karamitaheri, M. Pourfath, R. Faez, and H. Kosina, *IEEE Trans. Electron Devices* **60**, 2142 (2013).
- <sup>44</sup>M. Luisier, *Phys. Rev. B* **86**, 245407 (2012).
- <sup>45</sup>Z. Guo, D. Zhang, and X.-G. Gong, *Appl. Phys. Lett.* **95**, 163103 (2009).
- <sup>46</sup>A. Cao, *J. Appl. Phys.* **111**, 083528 (2012).
- <sup>47</sup>C. Yu and G. Zhang, *J. Appl. Phys.* **113**, 044306 (2013).
- <sup>48</sup>M. Park, S.-C. Lee, and Y.-S. Kim, *J. Appl. Phys.* **114**, 053506 (2013).
- <sup>49</sup>W. J. Evans, L. Hu, and P. Keblinski, *Appl. Phys. Lett.* **96**, 203112 (2010).
- <sup>50</sup>Y. Wang, B. Qiu, and X. Ruan, *Appl. Phys. Lett.* **101**, 013101 (2012).
- <sup>51</sup>J.-W. Jiang, J. Lan, J.-S. Wang, and B. Li, *J. Appl. Phys.* **107**, 054314 (2010).
- <sup>52</sup>U. Ray and G. Balasubramanian, *Chem. Phys. Lett.* **599**, 154 (2014).
- <sup>53</sup>A. V. Savin, Y. S. Kivshar, and B. Hu, *Phys. Rev. B* **82**, 195422 (2010).
- <sup>54</sup>J. Hu, S. Schiffl, A. Vallabhaneni, X. Ruan, and Y. P. Chen, *Appl. Phys. Lett.* **97**, 133107 (2010).
- <sup>55</sup>V. E. Dorgan, A. Behnam, H. J. Conley, K. I. Bolotin, and E. Pop, *Nano Lett.* **13**, 4581 (2013).
- <sup>56</sup>A. A. Balandin, *Nature Mater.* **10**, 569 (2011).
- <sup>57</sup>G. Chen, *J. Nanopart. Res.* **2**, 199 (2000).
- <sup>58</sup>S. V. J. Narumanchi, J. Y. Murthy, and C. H. Amon, *J. Heat Transfer* **127**, 713 (2005).
- <sup>59</sup>J. Y. Murthy and S. R. Mathur, *J. Heat Transfer* **124**, 1176 (2002).
- <sup>60</sup>S. V. J. Narumanchi, J. Y. Murthy, and C. H. Amon, *J. Heat Transfer* **126**, 946 (2004).
- <sup>61</sup>R. Yang, G. Chen, M. Laroche, and Y. Taur, *J. Heat Transfer* **127**, 298 (2005).
- <sup>62</sup>S. Sinha, E. Pop, R. W. Dutton, and K. E. Goodson, *J. Heat Transfer* **128**, 638 (2006).
- <sup>63</sup>D. Baillis and J. Randrianalisoa, *Int. J. Heat Mass Transfer* **52**, 2516 (2009).
- <sup>64</sup>A. Nabovati, D. P. Sellan, and C. H. Amon, *J. Comput. Phys.* **230**, 5864 (2011).
- <sup>65</sup>Z. Aksamija and I. Knezevic, *Phys. Rev. B* **90**, 035419 (2014).
- <sup>66</sup>D. Terris, K. Joulain, D. Lemonnier, and D. Lacroix, *J. Appl. Phys.* **105**, 073516 (2009).
- <sup>67</sup>D. A. Broido, M. Malorny, G. Birner, N. Mingo, and D. A. Stewart, *Appl. Phys. Lett.* **91**, 231922 (2007).
- <sup>68</sup>L. Lindsay, D. A. Broido, and N. Mingo, *Phys. Rev. B* **82**, 115427 (2010).
- <sup>69</sup>L. Lindsay, D. A. Broido, and N. Mingo, *Phys. Rev. B* **83**, 235428 (2011).
- <sup>70</sup>L. Lindsay, W. Li, J. Carrete, N. Mingo, D. A. Broido, and T. L. Reinecke, *Phys. Rev. B* **89**, 155426 (2014).
- <sup>71</sup>S. Mazumder and A. Majumdar, *J. Heat Transfer* **123**, 749 (2001).
- <sup>72</sup>J. Randrianalisoa and D. Baillis, *J. Heat Transfer* **130**, 072404 (2008).
- <sup>73</sup>A. Mittal and S. Mazumder, *J. Heat Transfer* **132**, 052402 (2010).
- <sup>74</sup>J.-P. M. Péraud and N. G. Hadjiconstantinou, *Phys. Rev. B* **84**, 205331 (2011).
- <sup>75</sup>K. Kukita and Y. Kamakura, *J. Appl. Phys.* **114**, 154312 (2013).
- <sup>76</sup>K. Kukita, I. Adisuilo, and Y. Kamakura, *J. Comput. Electron.* **13**, 264 (2014).
- <sup>77</sup>Y. Chen, D. Li, J. R. Lukes, and A. Majumdar, *J. Heat Transfer* **127**, 1129 (2005).
- <sup>78</sup>D. Lacroix, K. Joulain, and D. Lemonnier, *Phys. Rev. B* **72**, 064305 (2005).
- <sup>79</sup>D. Lacroix, K. Joulain, D. Terris, and D. Lemonnier, *Appl. Phys. Lett.* **89**, 103104 (2006).
- <sup>80</sup>A. H. Davoody, E. B. Ramayya, L. N. Maurer, and I. Knezevic, *Phys. Rev. B* **89**, 115313 (2014).
- <sup>81</sup>S. Wolf, N. Neophytou, and H. Kosina, *J. Appl. Phys.* **115**, 204306 (2014).
- <sup>82</sup>M.-S. Jeng, R. Yang, D. Song, and G. Chen, *J. Heat Transfer* **130**, 042410 (2008).
- <sup>83</sup>H. Hamzeh and F. Aniel, *J. Appl. Phys.* **109**, 063511 (2011).
- <sup>84</sup>W. R. Deskins and A. El-Azab, *Model. Simul. Mater. Sci. Eng.* **21**, 025013 (2013).
- <sup>85</sup>T. Hori, G. Chen, and J. Shiomi, *Appl. Phys. Lett.* **104**, 021915 (2014).
- <sup>86</sup>V. Jean, S. Fumeron, K. Termentzidis, S. Tutashkonko, and D. Lacroix, *J. Appl. Phys.* **115**, 024304 (2014).
- <sup>87</sup>R. Peterson, *J. Heat Transfer* **116**, 815 (1994).
- <sup>88</sup>D. G. Cahill, W. K. Ford, K. E. Goodson, G. D. Mahan, A. Majumdar, H. J. Maris, R. Merlin, and S. R. Phillpot, *J. Appl. Phys.* **93**, 793 (2003).
- <sup>89</sup>D. Lacroix, K. Joulain, D. Terris, and D. Lemonnier, *J. Phys.: Conf. Ser.* **92**, 012078 (2007).
- <sup>90</sup>E. B. Ramayya, L. N. Maurer, A. H. Davoody, and I. Knezevic, *Phys. Rev. B* **86**, 115328 (2012).
- <sup>91</sup>J. M. Ziman, *Electrons and Phonons: The Theory of Transport Phenomena in Solids* (Clarendon Press, Oxford, 1960).
- <sup>92</sup>J. Maultzsch, S. Reich, C. Thomsen, H. Requardt, and P. Ordejón, *Phys. Rev. Lett.* **92**, 075501 (2004).
- <sup>93</sup>M. Mohr, J. Maultzsch, E. Dobardžić, S. Reich, I. Milošević, M. Damnjanović, A. Bosak, M. Krisch, and C. Thomsen, *Phys. Rev. B* **76**, 035439 (2007).
- <sup>94</sup>L. Malard, M. Pimenta, G. Dresselhaus, and M. Dresselhaus, *Phys. Rep.* **473**, 51 (2009).
- <sup>95</sup>R. Saito, G. Dresselhaus, and M. S. Dresselhaus, *Physical Properties of Carbon Nanotubes* (Imperial College Press, London, 1998).
- <sup>96</sup>N. W. Ashcroft and N. D. Mermin, *Solid State Physics* (Saunders College, Philadelphia, 1976).
- <sup>97</sup>R. Sahoo and R. R. Mishra, *J. Exp. Theor. Phys.* **114**, 805 (2012).
- <sup>98</sup>A. Grüneis, R. Saito, T. Kimura, L. Cañado, M. Pimenta, A. Jorio, A. Souza Filho, G. Dresselhaus, and M. Dresselhaus, *Phys. Rev. B* **65**, 155405 (2002).
- <sup>99</sup>P. G. Klemens, *J. Wide Bandgap Mater.* **7**, 332 (2000).
- <sup>100</sup>Z. Wang, R. Xie, C. T. Bui, D. Liu, X. Ni, B. Li, and J. T. L. Thong, *Nano Lett.* **11**, 113 (2011).
- <sup>101</sup>C. Kittel, *Introduction to Solid State Physics*, 8th ed. (John Wiley & Sons, Inc., New York, 2004).
- <sup>102</sup>G. Gilat and L. Raubenheimer, *Phys. Rev.* **144**, 390 (1966).
- <sup>103</sup>T. Klitsner, J. VanCleve, H. Fischer, and R. Pohl, *Phys. Rev. B* **38**, 7576 (1988).
- <sup>104</sup>W. Cai, A. L. Moore, Y. Zhu, X. Li, S. Chen, L. Shi, and R. S. Ruoff, *Nano Lett.* **10**, 1645 (2010).
- <sup>105</sup>C. Faugeras, B. Faugeras, M. Orlita, M. Potemski, R. R. Nair, and A. K. Geim, *ACS Nano* **4**, 1889 (2010).

- <sup>106</sup>K. Yoon, G. Hwang, J. Chung, H. G. Kim, O. Kwon, K. D. Kihm, and J. S. Lee, *Carbon* **76**, 77 (2014).
- <sup>107</sup>K. Saito, J. Nakamura, and A. Natori, *Phys. Rev. B* **76**, 115409 (2007).
- <sup>108</sup>E. Muñoz, J. Lu, and B. I. Yakobson, *Nano Lett.* **10**, 1652 (2010).
- <sup>109</sup>H. Tomita and J. Nakamura, *J. Vac. Sci. Technol., B* **31**, 04D104 (2013).
- <sup>110</sup>B. Kong, S. Paul, M. Nardelli, and K. Kim, *Phys. Rev. B* **80**, 033406 (2009).
- <sup>111</sup>X. Jia, M. Hofmann, and V. Meunier, *Science* **323**, 1701 (2009).
- <sup>112</sup>K. Kim, S. Coh, C. Kisielowski, M. F. Crommie, S. G. Louie, M. L. Cohen, and A. Zettl, *Nat. Commun.* **4**, 2723 (2013).
- <sup>113</sup>P. Koskinen, S. Malola, and H. Häkkinen, *Phys. Rev. Lett.* **101**, 115502 (2008).
- <sup>114</sup>Ç. Ö. Girit, J. C. Meyer, R. Ermi, M. D. Rossell, C. Kisielowski, L. Yang, C.-H. Park, M. F. Crommie, M. L. Cohen, S. G. Louie, and A. Zettl, *Science* **323**(5922), 1705–1708 (2009).
- <sup>115</sup>J. Wang, X.-M. Wang, Y.-F. Chen, and J.-S. Wang, *J. Phys.: Condens. Matter* **24**, 295403 (2012).
- <sup>116</sup>P. Klemens and D. Pedraza, *Carbon* **32**, 735 (1994).
- <sup>117</sup>X. Li, W. Cai, J. An, S. Kim, J. Nah, D. Yang, R. Piner, A. Velamakanni, I. Jung, E. Tutuc, S. K. Banerjee, L. Colombo, and R. S. Ruoff, *Science* **324**, 1312 (2009).
- <sup>118</sup>A. Y. Serov, Z.-Y. Ong, and E. Pop, *Appl. Phys. Lett.* **102**, 033104 (2013).
- <sup>119</sup>N. Petrone, C. R. Dean, I. Meric, A. M. van der Zande, P. Y. Huang, L. Wang, D. Muller, K. L. Shepard, and J. Hone, *Nano Lett.* **12**, 2751 (2012).
- <sup>120</sup>G.-H. Lee, R. C. Cooper, S. J. An, S. Lee, A. van der Zande, N. Petrone, A. G. Hammerberg, C. Lee, B. Crawford, W. Oliver, J. W. Kysar, and J. Hone, *Science* **340**, 1073 (2013).
- <sup>121</sup>I. Vlassioux, S. Smirnov, I. Ivanov, P. F. Fulvio, S. Dai, H. Meyer, M. Chi, D. Hensley, P. Datskos, and N. V. Lavrik, *Nanotechnology* **22**, 275716 (2011).